NASA TECHNICAL NOTE

NASA TN D-8308

NASA TN D-8308

LOW-PERIGEE AERODYNAMIC HEATING DURING ORBITAL FLIGHT OF AN ATMOSPHERE EXPLORER

Paul S. Caruso, Jr., and Charles R. Naegeli

Goddard Space Flight Center
Greenbelt, Md. 20771

NATIONAL AERONAUTICS AND SPACE ADMINISTRATION · WASHINGTON, D. C. · SEPTEMBER 1976

1. Report No. NASA TN D-8308	2. Government Accession No.	3. Recipient's Catalog No.
4. Title and Subtitle Low-Perigee Aerodynamic Heating During Orbital Flight of an Atmosphere Explorer		5. Report Date September 1976
		6. Performing Organization Code 320
7. Author(s) Paul S. Caruso, Jr. and Charles R. Naegeli		8. Performing Organization Report No. G-76102
9. Performing Organization Name and Address Goddard Space Flight Center Greenbelt, Maryland 20771		10. Work Unit No.
		11. Contract or Grant No.
12. Sponsoring Agency Name and Address National Aeronautics and Space Administration Washington, D.C. 20546		13. Type of Report and Period Covered Technical Note
		14. Sponsoring Agency Code

15. Supplementary Notes

16. Abstract

This document presents the results of an extensive, low-perigee orbital aerodynamic heating study undertaken in support of the Atmosphere Explorer -C Temperature Alarm. Topics treated include state of the art of low-density, high-speed flows, some models of the Earth's atmosphere, external flow-field definition, thermodynamic and transport properties of atmospheric gases, the accommodation coefficient, orbital thermal environment, and correlation of theory and measurements. Aerodynamic heating rates are determined for eight selected orbits by means of a reduced, analytical model verified by both ground test and flight data. These heating rates are compared with classical free-molecule and first-order collision regime values.

17. Key Words (Selected by Author(s)) Aerodynamic heating, High-speed flows, Orbital thermal environment	18. Distribution Statement Unclassified—Unlimited CAT. 34		
19. Security Classif. (of this report) Unclassified	20. Security Classif. (of this page) Unclassified	21. No. of Pages 60	22. Price* $4.25

All measurement values are expressed in the International System of Units (SI) in accordance with NASA Policy Directive 2220.4, paragraph 4.

CONTENTS

NOTATION

A	surface area of the tungsten resistance-wire thermometer (RWT)
A_p	projected area of the tungsten RWT = 0.221 cm²
C_{mp}	most probable particle speed in the free stream (m/s)
C_p	specific heat of the free-stream gas at constant pressure (J/kmole K)
C_v	specific heat of the free-stream gas at constant volume (J/kmole K)
D	diameter of the AE-C spacecraft = 1.36 m
E_i	incident energy of the gas stream per unit surface area per second
E_r	reflected or reemitted energy carried away by the molecules as they leave the body
E_w	energy that the reemitted or reflected stream would have if all the incident molecules were reemitted with a Maxwellian velocity distribution corresponding to the surface temperature
e	the base of the natural logarithms
erf ( )	error function defined as erf $(\chi) = \dfrac{2}{\sqrt{\pi}} \displaystyle\int_0^\chi e^{-\chi^2} \, d\chi$
h_∞	average convective heat-transfer coefficient based on free-stream conditions (W/m² K)
h^*	average convective heat-transfer coefficient based on flight data (W/m² K)
K^*	thermal conductance at the Vespel supports = 0.145 mW/K
k_∞	thermal conductivity of the free-stream gas (W/m K)
Kn_∞	free-stream Knudsen number
Kn_0	Knudsen number based on stagnation conditions

Kn_w	Knudsen number based on wall conditions
L	spacecraft length = 1.14 m
M	mean molecular weight of air (kgm/kgm-mole)
N	Avogadro's number = 6.02257×10^{26} (kgm-mole)^1
N^*	number of altitude points included in the aerodynamic heating cubic curve fit process
Nu_∞	free-stream Nusselt number
Nu^*	Nusselt number based on flight data
$\dot{Q}_{ALBEDO}$	Earth albedo flux incident on the RWT (mW/cm^2)
$\dot{Q}_{IR}$	earthshine flux incident on the RWT (mW/cm^2)
$\dot{Q}_{SOLAR}$	direct solar flux incident on the RWT (mW/cm^2)
$\dot{q}_{AERO}$	absorbed aerodynamic flux per unit projected area (mW/cm^2)
$\dot{q}^{(1)}_{AERO}$	unsmoothed calculated aerodynamic heating rate at each selected altitude (mW/cm^2)
$\dot{q}^{(2)}_{AERO}$	least-squares cubic curve fit aerodynamic heating rate at each selected altitude (mW/cm^2)
$\dot{q}_{FM}$	free-molecular heating rate (mW/cm^2)
$\dot{q}_{FM\ MESA}$	free-molecular heating rate based on drag measurements from the AE-C MESA accelerometer (mW/cm^2)
$\dot{q}_{FM\ 1966}$	free-molecular heating rate based on density values from the 1966 Standard Atmosphere Supplements (mW/cm^2)
$\dot{q}_{NFM}$	near free-molecular heating rate (mW/cm^2)
$\dot{q}_{NFM\ MESA}$	near free-molecular heating rated based on $\dot{q}_{FM\ MESA}$ (mW/cm^2)
$\dot{q}_{NFM\ 1966}$	near free-molecular heating rate based on $\dot{q}_{FM\ 1966}$ (mW/cm^2)

$\dot{q}_{RAD}$	radiation error per unit projected area (mW/cm^2)
R	Universal gas constant $= 8314.34$ J/kmole K
R_{E_∞}	free-stream Reynolds number
r	recovery factor
S_∞	speed ratio based on free-stream conditions
S_0	speed ratio based on stagnation conditions
S_{T_∞}	free-stream Stanton number
S_T*	Stanton number based on flight data
T_∞	free-stream atmospheric-gas temperature (K)
T_B	body-surface temperature (K)
T_0	atmospheric-gas stagnation temperature (K)
T_R	recovery temperature of the body (K)
T_{SH}	temperature of the sensor housing measured in orbit by a flight thermistor (K)
T_{SP}	space background temperature $= 0$ K
T_W	temperature of the tungsten RWT measured in orbit (K)
$T*$	temperature of the Vespel support (K)
U	spacecraft velocity (m/s)
$\overline{V}$	mean molecular speed (m/s)
$\overline{\alpha}$	thermal accommodation coefficient
α_S	solar absorptivity of the tungsten RWT $= 0.85$
γ	ratio of specific heats of the atmospheric gas

ϵ	infrared absorptivity or emissivity of the tungsten RWT = 0.025
θ	angle the free-stream velocity vector makes with the solid surface
θ_v	characteristic temperature for vibration
λ_∞	mean free path in the free stream (m)
λ_0	mean free path based on stagnation conditions (m)
ν_∞	kinematic coefficient of viscosity (m^2/s)
ϕ	ratio of $\dot{q}_{NFM}$ to $\dot{q}_{FM}$ as defined by equation (24)
ρ_∞	free-stream atmospheric density (kgm/m^3)
σ	effective collision diameter of a molecule of air = 3.65 x 10^{-10} m
$\overline{\sigma}$	uncertainty in the calculated aerodynamic heating rate (mW/cm^2)
σ^*	Stefan-Boltzmann constant

LOW-PERIGEE
AERODYNAMIC HEATING DURING ORBITAL FLIGHT
OF AN ATMOSPHERE EXPLORER

Paul S. Caruso, Jr. and Charles R. Naegeli
Goddard Space Flight Center
Greenbelt, Maryland

INTRODUCTION

The primary objective of the Atmosphere Explorer (AE) program is flight measurement of aeronomic quantities within the Earth's thermosphere, a region of the upper atmosphere between 100 and 300 km. With a complement of three spacecraft (AE-C, launched in late 1973; and AE-D and AE-E, launched in late 1975), data are being collected over a wide range of inclination angles (22 to 98 degrees) and over all latitudes with incumbent seasonal and diurnal variations. A detailed description of the spacecraft and experiments is contained in a special issue of *Radio Science* (Reference 1).

The AE-C spacecraft was launched on December 15, 1973, at 2218 PST. The orbit was inclined 68 degrees to the Equator with initial perigee of 155 km and apogee of 4297 km. Because the spacecraft contains a unique orbit-adjust propulsion system, both perigee and apogee altitudes can be, and have been, incrementally adjusted. The AE-C spacecraft has been operated at a spin rate of 4 revolutions per minute (rpm) with perigee heights as low as 130 km and despun at 1 revolution per orbit (rpo) for perigee heights as low as 135 km. During the first 6 months of the AE-C mission, two perigee lowerings were executed to bring the spacecraft down to 130 km in increments of approximately 5 km. It was during these maneuvers, in both spinning and despun modes for a period of 15 minutes on either side of perigee, that the Temperature Alarm (TAL-C) gathered the bulk of engineering data presented in this report. Further TAL-C instrument details are contained in References 2, 3, and 4.

Because the three spacecraft dip into the sensible portion of the Earth's atmosphere, they experience aerodynamic heating and pressure effects. The transient aerodynamic heating component is sizable with respect to direct solar, albedo, and earthshine fluxes and therefore impacts both the spacecraft and the experiment designs. Experiment geometries give rise to a two-fold rarefied flow problem: an external flow and an internal flow. Internal flow refers to particle motion inside the experiments and will not be treated here. External flow is generated by particle motion around the spacecraft at orbital velocity and sets the boundary conditions for the internal flow. The external flow field is defined in later sections of this report.

Because low-altitude satellite interaction studies are a new area of concern for spacecraft design evaluation, this document reviews the state of the art of appropriate analytical and experimental aerodynamic techniques and some models of the Earth's atmosphere, defines the external flow field, the accommodation coefficient, and the orbital thermal environment, and presents the governing equations used for analysis. Finally, empirical and theoretical aerodynamic heating rates of atmospheric constituents on pure tungsten wire are compared, and the magnitudes of important dimensionless groups such as Knudsen number, speed ratio, Reynolds number, Nusselt number, Stanton number, and recovery factor are indicated for the eight selected orbits.

STATE OF THE ART OF LOW-DENSITY, HIGH-SPEED FLOW

Reentry vehicles encounter a broad range of flow regimes—from the free molecular at near vacuum conditions to the continuum regime at high density. When the flow is characterized by single collisions between free-stream gas particles and the vehicle surface, the flow is called free molecular (Reference 5). By virtue of the well-established laws of molecular motion (kinetic theory), this regime is readily susceptible to analysis and has been thoroughly examined with respect to both aerodynamic and thermodynamic phenomena (Reference 6). Likewise, continuum aerodynamics used at low altitudes is also well-developed and essentially relies on the Navier-Stokes equations with appropriate boundary and initial conditions. The large region between these two limiting flow regimes is difficult to treat analytically. Two rigorous analytical approaches have received attention in past work.

Briefly, the first approach consists of applying correction terms to the Navier-Stokes continuum equations and boundary conditions, the first approximation resulting in a set of higher-order equations (e.g., the Burnett equations). The other approach is to attempt to solve the Boltzmann equation for the molecular velocity distribution, which, in effect, results in obtaining correction terms to the Maxwell velocity-distribution equations. Both of these methods are essentially perturbation methods. In the first approach, solutions are obtained in terms of power series of the Knudsen number, and, in the second method, solutions are obtained in terms of the reciprocal of the Knudsen number. Both methods will fail for Knudsen numbers of the order of unity (Reference 6).

Semiempirical equations have also been formulated to predict heat transfer, shear, drag, lift, and pressure distribution for blunt bodies operating in the transition flow regime. These equations "are derived from models based on simplified kinetic theory; the structure of the equations is such that they are asymptotically correct at the free-molecule and continuum extremes, and this tends to place bounds on errors resulting from a simplified analysis" (Reference 7).

Recently, a numerical method called the Monte Carlo direct-simulation technique has been developed for the study of rarefied gas flows. It has been shown to be a practical way of treating high-speed flows in the entire transition regime (Reference 8). In the total flow field, a relatively small number of molecules (of the order of several thousand) compared to the

2

number in an actual gas is set in uniform motion in a field of sufficient size to contain the disturbance caused by the body. The molecules are distributed uniformly in space, and their velocity components are assigned by sampling from a distribution which is Maxwellian about the free-stream velocity. The molecular paths between collisions are computed exactly, but collisions are treated statistically. The calculation procedure consists of holding all molecules motionless for a time interval while collisions are computed in the field, and then allowing the molecules to move with their new velocities for another time interval. After a sufficient time interval has passed for the mean flow to traverse a distance of a few body lengths, the flow is considered to be sufficiently close to the steady state. In this manner, a collection of simulated molecules numbering many orders of magnitude less than those in the real gas behaves like the collection of real molecules, and, by continuing the calculation for a sufficiently long time, an accurate description of the flow field and surface properties can be obtained (Reference 9).

Although many analytical techniques are available for rarefied gasdynamic calculations, they all have certain inherent limitations. Gasdynamic predictions are dependent on a proper choice of the following (Reference 5):

- The chemical and physical structure of the Earth's atmosphere, including the relative proportions of monatomic and diatomic gases together with charged and uncharged particles

- The thermodynamic, transport, and optical properties of atmospheric constituents such as density, specific heats, thermal conductivity, viscosity, and most probable particle speed

- The flow field surrounding the vehicle

- Energy transfer processes which are influenced by ionization, dissociation, specular versus diffuse particle reflection dynamics, and density buildup

Because of these factors, any gasdynamics analysis performed for a low-perigee spacecraft encounter with the atmosphere requires a corresponding uncertainty analysis to place some bandwidth on predicted values.

A great number of gasdynamics test facilities are in operation and cover a spectrum of Mach-number, Reynolds-number, and temperature simulation. Such facilities include conventional wind tunnels, arc tunnels, constricted-arc tunnels, rocket sleds, hotshot tunnels, ballistic and counterflow ranges, shock tubes, and shock tunnels. References 5 and 10 contain detailed descriptions of these facilities. Gasdynamic tests are usually conducted to obtain data for establishing or verifying analytical techniques, to determine heat-transfer levels and distributions for complex geometries, and to study gas and flow-field characteristics.

Many different types of test facilities are available, but simultaneous duplication of speed, enthalpy, density, and gas chemistry in any one of these is most unlikely. In addition, even in carefully designed tests, measurement errors and/or discrepancies between theory and experiment can occur.

3

No aerodynamic test facility now exists that can adequately duplicate the AE spacecraft velocity, free-stream density, and composition of the Earth's atmosphere between altitudes of 120 and 180 km. Moreover, hypersonic wind tunnels that approach the desired flight parameters are size-limited, and scale modeling would therefore be required. Finally, cost, schedule, and contamination-control constraints make aerodynamic testing of the spacecraft and experiments prohibitive.

Because convective heating rates for low-perigee orbital flight can be duplicated, heat-flux calibration tests in an aerodynamic molecular-beam chamber were performed on two Temperature Alarm sensor heads under conditions of partial simulation. Calibration test details are reported in Reference 3. Note that the Temperature Alarm is not an experiment but, rather, an engineering instrument designed to provide a thermal measurement indicative of the temperature of low-mass experiment components, thus providing information to assist in the decision process regarding real-time perigee maneuvers.

MODELS OF THE EARTH'S ATMOSPHERE

Variation of pressure, density, and temperature of the Earth's atmosphere with altitude has received much consideration over the years. Detailed tabulations of these parameters are given in the U.S. Standard Atmospheres (References 11, 12, and 13). The 1962 U.S. Standard Atmosphere presents the year-round mean properties for middle-latitude locations, with seasonal and global variations given in the 1966 U.S. Standard Atmosphere Supplements.

Because atmospheric conditions change with latitude, longitude, altitude, and solar and geomagnetic activity, computer models have been developed to predict density, chemical composition, temperature, and molecular mass for given times. Two well-known models used for prediction in the 120- to 1000-km range are the Jacchia model and the Harris and Priester model (CIRA 1965). These models assume constant boundary conditions at 120 km (Reference 14). However, satellite and rocket data have shown considerable variations at 120 km and "as a result, these models, while relatively adequate at heights above 250 km, become progressively unrealistic as we proceed to lower heights" (Reference 15). Therefore, model usefulness is limited for the Atmosphere Explorer low-perigee environment study presented herein.

Because reasonable agreement exists between low-altitude density measurements by satellite (Reference 16) and the 1966 U.S. Standard Atmosphere Supplements (Spring/Fall Model, 1000 K Exospheric Temperature), the latter source of atmospheric density, temperature, and molecular mass as a function of altitude has been adopted to expedite the computations presented in this paper. For comparison, aerodynamic heating rates based on density measurements determined from the AE-C Accelerometer (MESA) experiment have also been computed for six of the eight orbits selected for analysis (F. A. Marcos, private communication, unpublished data from the Atmosphere Explorer-C Mission, June 1975).

4

A review of preliminary AE-C experiment data at altitudes between 130 and 200 km indicates that the predominant species (neutral gases) in order of decreasing importance are:

1. $N_2 \sim 10^{16}$ m^{-3}

2. $O \sim 10^{16}$ m^{-3}

3. $O_2 \sim 10^{16}$ m^{-3}

4. $Ar \sim 10^{14}$ m^{-3}

5. $He \sim 10^{12}$ m^{-3}

On the basis of these estimates, it has been assumed that atmospheric constituents in the altitude range specified above behave as a diatomic gas does. This assumption affects the values of specific heats used in subsequent calculations.

EXTERNAL FLOW-FIELD DEFINITION

Flow-field characteristics for a body in a high-speed, rarefied gas stream are basically determined by calculation of the Knudsen number and the speed ratio. The Knudsen number (Kn) is the ratio of the mean free path of the gas (λ) to a characteristic length. This characteristic length may be a body dimension or a shock-layer thickness. The speed ratio (S) arises in place of the Mach number and is the ratio of the body velocity (U) to the most probable speed (C_{mp}) of a molecule in the free stream. The most probable speed is that corresponding to the radius of the spherical shell in velocity space containing the largest number of representative points. In simple terms, more molecules have the speed C_{mp} than any other speed (Reference 17).

The AE-C spacecraft (figure 1) is a 16-sided convex body that approximates a short, right-circular cylinder. In flight, the spacecraft is always aligned with the velocity vector normal to the cylinder axis. For cylindrical configurations in cross flow, it is generally accepted that the characteristic dimension is the diameter (D). Thus, in the free stream,

$$Kn_\infty = \frac{\lambda_\infty}{D} \tag{1}$$

where $D \approx 1.36$ m for the AE-C configuration. Because the AE-C length to diameter ratio is small ($L/D \approx 0.84$), some flow irregularities can be expected at the edges of the spacecraft. The foregoing Knudsen number definition also applies to the Temperature Alarm because the instrument sensor head protrudes only about 0.1 cm from the main spacecraft surface; therefore, the spacecraft itself determines the flow regime for the TAL-C sensors. In addition, the instrument is located near the center of the spacecraft and is therefore in an ideal location for keeping edge effects to a minimum.

SCIENTIFIC EXPERIMENTS
CONTAINING LOW-MASS
ELEMENTS

TEMPERATURE
ALARM (TAL-C)
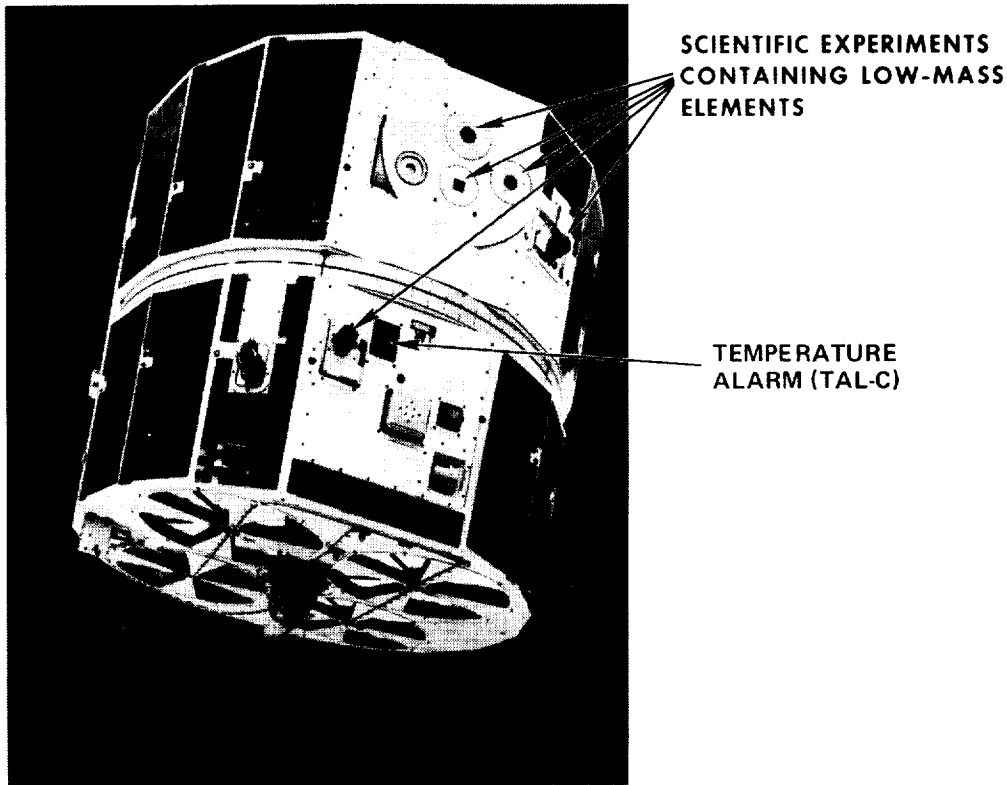
Figure 1. Atmosphere Explorer-C (AE-C) spacecraft.

As mentioned previously, the two best-defined flow regimes are the continuum and the free-molecular flow regimes. For continuum flow, the Knudsen number is much less than unity, whereas, for free-molecular flow, it is much greater than unity. Between these two limiting cases lie several intermediate regimes in which viscous effects may or may not be important, and the flow may or may not rightfully be considered rarefied (Reference 18).

To calculate the free-stream Knudsen numbers (Kn_∞) for the AE-C spacecraft and TAL-C, the mean free path as a function of perigee altitude must first be computed. From kinetic theory (References 12 and 19), the mean free path (λ_∞) is given by the relationship

$$\lambda_\infty = \frac{M}{\sqrt{2\pi} \, N \, \sigma^2 \, \rho_\infty}$$

(2)

Free-stream Knudsen number versus AE-C low-perigee altitudes is illustrated in figure 2.

The requirement that the free-stream Knudsen number be much greater than 1 is not always sufficient to ensure free-molecular flow. One rationale is that, if the body is cool, the mean free path near the body (λ_w) will be less than λ_∞. Thus, to ensure free-molecular flow in this case requires that $Kn_w \gg 1$ (Reference 18). Because the AE-C spacecraft and TAL-C

6

are cool-walled bodies (that is $T_B < T_\infty$, where T_B is the temperature of the spacecraft external solar array, and T_∞ is the free-stream gas temperature before collision with the spacecraft), it appears at first glance that use of wall conditions for definition of AE-C spacecraft and TAL-C flow regimes be considered. However, it has been shown that drag data are not well-correlated by this approach. Rather, the data correlate with theory when stagnation conditions are used (Reference 20). In high enthalpy flows (high flight velocities), particles are not well-accommodated to the surface and act as if they have a stagnation temperature, T_o. This does not mean that the body is at the stagnation temperature of the gas but that there is a microscopic gas-surface effect at the spacecraft boundary.

In Reference 20, it has been shown that, to second order, the mean free path based on stagnation conditions (λ_0) is given by the expression

$$\frac{\lambda_\infty}{\lambda_o} = \frac{(2)^{3/2}}{3\pi} \left[\sqrt{\pi} S_o + 1 + \frac{\sqrt{\pi}}{2S_o} \left(1 + \frac{T_\infty}{T_o} \right) \right] \tag{3}$$

where λ_∞ is given by the previous equation, and S_0 is the speed ratio based on the gas stagnation temperature. S_0 is calculated from

$$S_o = \frac{S_\infty}{\sqrt{T_o/T_\infty}} \tag{4}$$

$$S_\infty = \frac{U}{C_{mp}} \tag{5}$$

$$C_{mp} = \sqrt{\frac{2RT_\infty}{M}} \tag{6}$$

$$\text{and } \frac{T_o}{T_\infty} = 1 + \left(\frac{\gamma - 1}{\gamma} \right) S_\infty^2 \tag{7}$$

The expression for the ratio λ_∞/λ_0 in equation 3 is applicable for blunt bodies with $S_\infty > 2$ and thus can be used for the AE-C spacecraft and TAL-C gasdynamic analyses for all perigee heights encountered. These quantities have been calculated as a function of altitude for eight selected low-perigee passes (Appendix).

It now remains to define the flow regimes encountered by the AE-C spacecraft and TAL-C during typical low-perigee maneuvers. For the eight selected orbits, Kn_∞ varies from approximately 10 to 79, and Kn_0 varies from 7 to 54 between altitudes of 135.7 and 180 km, respectively. Comparison of these calculated Knudsen numbers with flow-field definitions given by Hayes and Probstein (Reference 18) and Wuest and Koppenwallner (Reference 21) indicates that the spacecraft and TAL-C are probably in the free-molecular flow regime at the upper end of the altitude range stated above and possibly in the first-order collision regime toward the lower end of the above altitude range. By way of explanation, in free-molecular flow analyses, all intermolecular collisions are neglected, whereas, in the first-order collision regime, free-stream molecules may have one collision with reflected or emitted molecules and all subsequent collisions are neglected.

An alternate representation of flow regimes, developed by Klett (Reference 22), is illustrated in figure 3. This method of flow-field determination requires the calculation of the free-stream Reynolds number by

$$RE_\infty = \frac{UD}{\nu_\infty} \tag{8}$$

$$\text{with } \nu_\infty = 1/3 \, \overline{V} \lambda_\infty \tag{9}$$

$$\text{and } \overline{V} = \sqrt{\frac{8\,R\,T_\infty}{\pi M}} \tag{10}$$

The mean molecular speed $(\overline{V})$ is equal to 1.128 times the most probable particle speed defined earlier. Free-stream Reynolds number versus altitude is illustrated in figure 4 for a typical low-perigee pass.

Examination of the pictorial flow-field definition of figure 3 reveals that the AE-C spacecraft and TAL-C are in the free-molecular flow regime for altitudes above 145 km and in nearly free-molecular flow (first-order collision regime) from 145 km down to 135.7 km. This determination of flow regimes corresponds well with that based on Kn_∞ and Kn_0 specified previously.

The foregoing conclusions about the external flow field permit the use of equations derived from kinetic theory for calculation of transport and thermodynamic properties of atmospheric gases, as well as determination of in-flight orbital aerodynamic heating rates.

THERMODYNAMIC AND TRANSPORT PROPERTIES OF ATMOSPHERIC GASES

Thermodynamic properties such as free-stream density and temperature have been obtained from the sources previously described. Because preliminary AE-C results indicate that the
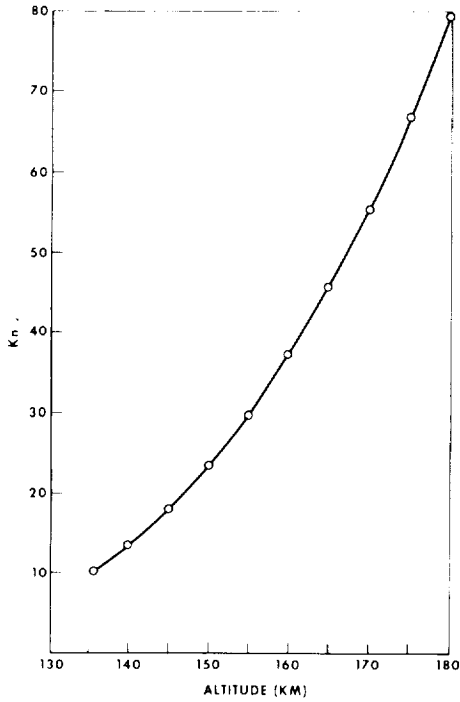
Figure 2. Typical Knudsen number versus altitude profile for a low-perigee pass.
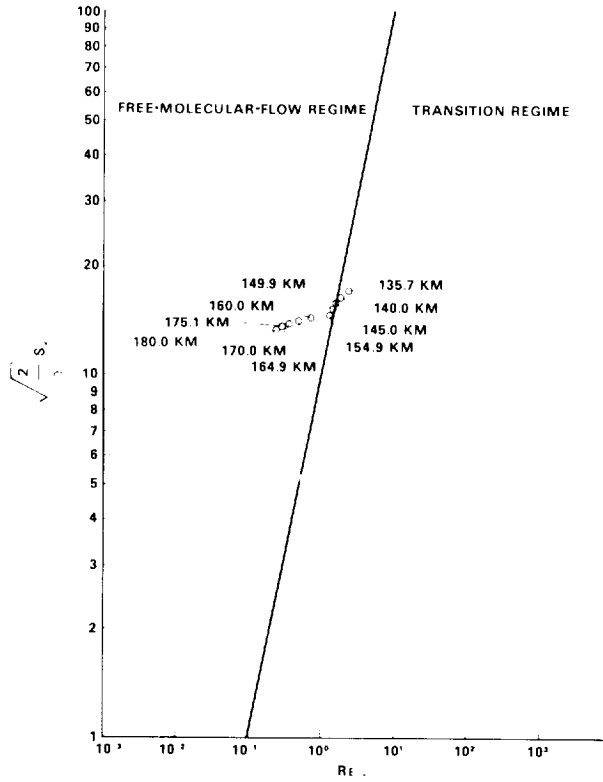
Figure 3. Speed ratio/Reynolds number field for a typical AE-C despun low-perigee pass.

neutral gas mixture is predominantly diatomic and that N_2 is the single most important constituent, total specific heat of the gas at constant volume is given by the expression (Reference 23):

$$C_v = R \left\{ \frac{5}{2} + \left[\frac{\theta_v/2T_\infty}{\sinh \ (\theta_v/2T_\infty)} \right]^2 \right\} \tag{11}$$

where θ_v is the characteristic temperature for vibration and is equal to 3390 K for N_2. From the ideal gas law, the specific heat at constant pressure (C_p) is then found from

$$C_p = C_v + R \tag{12}$$

The ratio of specific heats (γ) is defined as

$$\gamma = C_p/C_v \tag{13}$$

9
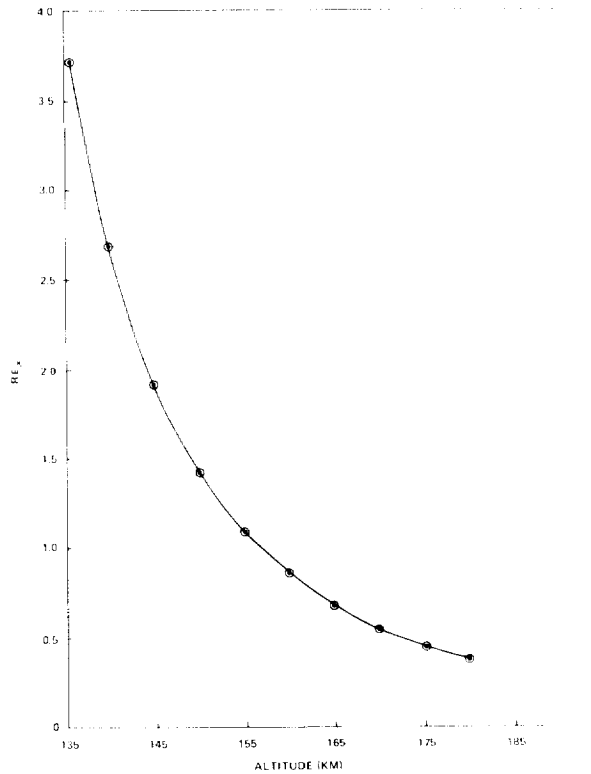
Figure 4. Reynolds number versus altitude
for a typical low-perigee pass.

Transport properties such as kinematic viscosity and thermal conductivity can be treated
from a molecular point of view. These properties are then explained in terms of the trans-
port across some imagined surface within the gas of momentum and energy by the molecules
crossing the surface. The viscosity of a gas arises not from any frictional forces between its
molecules, but rather from the fact that they carry momentum across a surface as a result
of their random thermal motion. Similarly, the gas thermal conductivity arises from the
fact that molecules also carry an excess of energy across a surface (Reference 17). The
relationship used to determine the kinematic viscosity of a rarefied gas has been presented
in equation 9. The thermal conductivity of free-stream atmospheric gases is approximated
from References 17 and 23.

$$k_\infty = \frac{\nu_\infty \rho_\infty C_v}{M} \tag{14}$$

The thermodynamic and transport properties defined above have also been tabulated in the
Appendix as a function of altitude for the eight selected orbits.

10

THE ACCOMMODATION COEFFICIENT

The many and varied missions of near-Earth and planetary-space probes during the past decade have caused additional emphasis to be placed on the relatively old problem of momentum and energy exchange between rarefied gas flows and the surfaces on which they impinge. The distinction between normal and tangential accommodation coefficients is used for calculating forces and moments in rarefied flow. For energy considerations, an overall accommodation coefficient is usually employed. In order to compute free- and near-free-molecular convective heat fluxes for the AE-C spacecraft and TAL-C tungsten resistance-wire thermometer, a knowledge of appropriate thermal accommodation coefficients is required because heat-flux magnitude is directly proportional to this quantity. The thermal accommodation coefficient $\bar{\alpha}$ is "a measure of the extent to which the mean energy of the molecules that hit the surface and are reflected or reemitted is accommodated toward an energy corresponding to the temperature of the wall" (Reference 18). In equation form,

$$\bar{\alpha} = \frac{E_i - E_r}{E_i - E_w} \tag{15}$$

Thus, if the gas molecules are assumed to hit a smooth, hard surface and leave with their normal velocity component reversed and their tangential velocity component unchanged (specular reflection process), $E_r = E_i$ and $\bar{\alpha} = 0$. On the other hand, if the molecules issue with a Maxwellian velocity distribution corresponding to a temperature close to that of the surface (diffuse reflection process), $E_r = E_w$ and $\bar{\alpha} = 1$.

For engineering surfaces, the diffuse assumption has proven to be more realistic, but specification of $\bar{\alpha}$ is a major difficulty because it is a function of many variables. Among these are: (1) molecular weight and structure of impinging gas molecules, (2) energy level of the incoming molecular stream, (3) surface orientation with respect to the gas stream, (4) physical structure of the solid surface (lattice structure, roughness), (5) presence of physically adsorbed or chemisorbed layers, and (6) temperature level of the solid surface (Reference 24).

Theory and limited experimental data suggest that the accommodation coefficient is significantly less than 1 for light gases, such as hydrogen and helium, that impinge on clean surfaces (References 25 and 26).

Both tangential and normal momentum-accommodation coefficients have been measured for N_2^+ ions striking aluminum surfaces at speeds ranging from slightly below to about twice Earth-satellite speed. The coefficients were shown to be strongly dependent on the incident particle energy with both components decreasing rapidly with energy in the range of interest for Earth satellites. Moreover, accommodation of the normal component of momentum decreased rapidly as the incidence angle approached the grazing angle. In contrast, accommodation of the tangential momentum increased as the incidence angle approached the grazing angle, but the effect of incidence angle on the tangential component was generally less than for the normal component (Reference 27). With respect to molecular reemission, distributions

of lobal form have been found for many gas and surface combinations and for various beam energies and surface temperatures, instead of the classical Knudsen cosine distribution. A systematic approach of the reflected maximum toward the surface has been observed as the energy of the incident stream is increased, and this event is accompanied by a systematic narrowing of the reflected lobe. "The position of the reflected maximum changes approximately as does the position of the specular direction for changes in the direction of the incident stream" (Reference 28).

When the incident energy of the impinging molecules is sufficiently large for the hard-sphere model to be valid, the mass ratio (mass of incoming molecules divided by the mass of surface molecules) will depend on the nature of the outermost layer of atoms on the surface, and not on the actual material used in constructing the surface. Because oxygen is fairly abundant at ground level and because atomic oxygen is one of the main atmospheric constituents at the orbital altitudes of near-Earth spacecraft, the surfaces of all metals except gold may be covered by at least one monolayer of adsorbed oxygen. For nonmetals and painted surfaces, the outermost layer of atoms is not easily defined (Reference 25). In addition, "surfaces covered by adsorbed gas films exhibit diffuse scattering behavior, yet may exhibit lobal scattering patterns when the gas film is removed by heating. Lobal patterns may [also] be observed on dirty surfaces when the energies of the incident particles are sufficiently high" (Reference 28).

The temperature level of the solid surface also has an effect on the degree of accommodation that takes place. "As the stagnation temperature of the incident molecules becomes large in comparison with the wall temperature (as is the case for the AE-C spacecraft and TAL-C tungsten resistance wire thermometers), there is less tendency for the temperature of a [gas] molecule to be adjusted toward that of the surface and it may be expected that the reflection then tends to be elastic, although not necessarily specular" (Reference 29). Experiments performed on surfaces at room temperature have shown a diffuse scattering of incident molecules, whereas, at high temperature, scattering was shown to be remarkably specular. The difference in these observed distributions between hot and cold surfaces is probably caused by the presence of adsorbed gaseous contaminants at low temperatures (Reference 30).

This brief review of the literature illustrates the complexity of quantifying the accommodation coefficient for spacecraft application. Cook (Reference 25) reports that the accommodation coefficient at the surface of most satellites probably exceeds 0.8 at altitudes up to about 400 km at all times of day and for all levels of solar activity. There are known exceptions to this general statement by Cook, however. Because the subject matter of this report concentrates on aerodynamic heating rates to a TAL-C 99.99-percent pure tungsten resistance-wire thermometer, some pertinent information is evaluated in the following. Hyson (Reference 31) states that, although $\bar{\alpha}$ is usually 0.9 for air on metal, it is much lower for tungsten [$\bar{\alpha} = 0.35$ for nitrogen on tungsten (Reference 32) and $\bar{\alpha} = 0.57$ for air on tungsten (Reference 33)]. Roberts (References 34 and 35) did extensive tests to measure accommodation coefficients of monatomic gases such as helium on tungsten wire. His experiments showed that the accommodation coefficient for a clean wire is considerably smaller than for a wire covered

with films of adsorbed gas. Moreover, the accommodation coefficient of a clean wire (cleaned by heating to a high temperature) "shows a definite drift with time. presumably owing to the gradual buildup of adsorbed films from residual impurities in the [test] gas" (Reference 34). He also showed experimentally, as Knudsen did, that the measured value of the accommodation coefficient increases as surface roughness increases. Some experimental data from Reference 34 are presented in table 1 for helium on tungsten where the test gas is essentially free of oxygen and nitrogen.

Table 1
Accommodation Coefficient of Helium on Tungsten

$\overline{\alpha}$ (Clean Surface)		$\overline{\alpha}$ (Dirty Surface)
Roughness	0.07	0.19
Increasing	0.12	0.40
	0.18	0.55

Results are also given for the variation of the accommodation coefficient of helium on tungsten for temperatures between 295 K and 79 K. At the latter temperature, the very low value of 0.025 was obtained. Results indicate that, if the observed variation continued down to absolute zero, the accommodation coefficient would approach zero because collisions of gas atoms with a solid surface become more and more nearly perfectly elastic (Reference 35). Although the Roberts' experimental data are not for a diatomic gas, they exhibit consistent trends that should be expected for atmospheric gases impinging on TAL-C tungsten wires at low-perigee altitudes.

EMPIRICAL ORBITAL AERODYNAMIC HEATING RATES FOR A TUNGSTEN WIRE

This section defines the orbital thermal environment for a tungsten resistance-wire thermometer (RWT) flying broadside to the free stream at orbital altitudes between 135 and 180 km, and establishes the techniques employed to determine orbital aerodynamic heating rates from RWT temperature data telemetered to the ground from the AE-C spacecraft. Eight orbits (211, 895, 911, 1352, 1371, 1375, 1558, and 2271) have been selected for analysis because flight data gathered during two perigee lowerings have shown that the above orbits are representative of the low-perigee phase of the mission. Finally, a heat balance for the RWT is established, and an error and uncertainty analysis is presented.

Orbital Thermal Environment

The TAL-C tungsten RWT receives the usual thermal radiative inputs from direct solar, albedo, and earthshine fluxes. These external radiative fluxes are typical for near-Earth-orbiting satellites and can be determined with reasonable accuracy from existing computer programs

13

with input based on actual flight attitude parameters. The All Planet Flux Program developed at NASA/GSFC (Reference 36) was employed for these calculations.

During one phase of the mission, however, the spacecraft dips into sensible regions of the Earth's atmosphere (130 to 180 km) and experiences appreciable transient free-molecular heating. The magnitude of this aerodynamic input is primarily a function of spacecraft velocity, atmospheric density, and the local accommodation coefficient. The spacecraft velocity, in turn, varies with the orbital parameters but is well known from tracking-station data. The atmospheric density varies to some degree with absence or presence of sunlight, as well as with solar and geomagnetic activity indices, but flight data from the AE-C accelerometer for orbits 895, 911, 1352, 1371, 1558, and 2271 have shown that density values from the 1966 U.S. Standard Atmosphere Supplements (Spring/Fall Model, 1000 K Exospheric Temperature) are adequate estimates for engineering heat-transfer calculations. Finally, the effective accommodation coefficient for atmospheric gases on tungsten can be determined by taking the ratio of the excess absorbed energy (the amount over and above that attributable to thermal radiation necessary to satisfy the heat balance of the tungsten wire) to the theoretical classical free-molecular limit.

Heat Balance for the RWT

Much effort has been expended to generate an acceptable thermal mathematical model for the TAL-C tungsten RWT. Analytical and test work has shown that the heat balance of a fine tungsten wire wrapped around more massive low-conductivity support pegs is conduction-dominated. Consequently, the sensitive parameters in the analysis relate to the conductive heat transfer between the wire grids and the support pegs and to the solar absorptivity of tungsten wire. The conductive coupling includes a contact resistance between the RWT and the Vespel support pegs, as well as an axial conduction along the length of the RWT. This coupling (K^*) was chosen so that the temperature response of the RWT predicted by the analytical model showed reasonable agreement with flight data from orbit 2271 (figure 5), and this value was used in all subsequent flight-data analysis. Another important parameter, the solar absorptivity (α_s) of fine tungsten wire, was determined from ground test data by comparing the amount of electrical power needed to achieve a certain RWT temperature with an equivalent amount of incident, simulated solar power at a known intensity needed to induce the same temperature.

Although the thermal capacitance of the support pegs was also determined during ground solar-simulation testing, there still remained an uncertainty as to the temperature/time response of the support pegs during orbital heating because the exact flight thermal loading, including absorbed aerodynamic heating, could not be simulated on the ground. However, because of the short duration of the orbital aerodynamic heating and because the temperature of the supports (T^*) can be determined at the onset and conclusion of aerodynamic heating, it was possible to approximate the temperature/time response of the supports as a straight line connecting these end points.

14
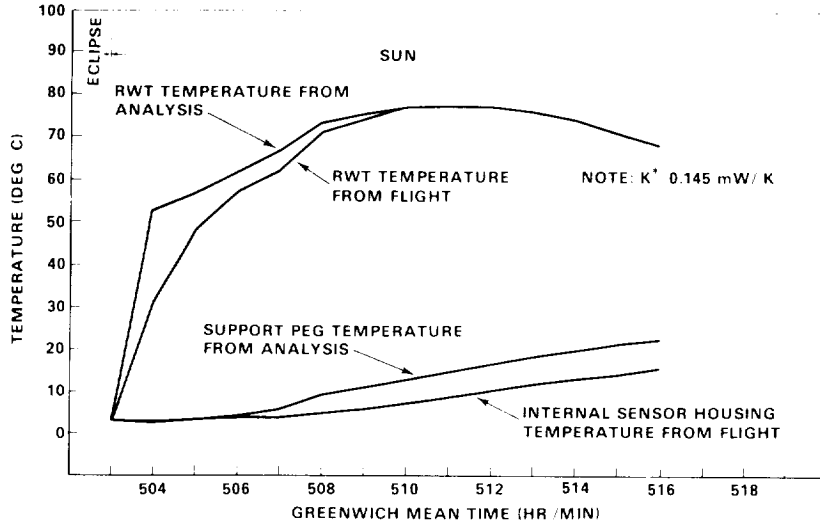
Figure 5. Comparison of flight and analytical temperature profiles based on
selected conductive coupling between RWT and support pegs.

Finally, the radiative exchange between the RWT and deep space, as well as between the RWT
and the sensor housing, was dropped from the analytical model because this total radiative
contribution to the heat balance of the RWT was minimal compared to other inputs (less than
10 percent of the total heat balance) and because the flux budgeted for these inputs fell far
short of the error associated with temperature-derived aerodynamic fluxes. A plot of power
versus steady-state temperature for an electrically heated RWT in a vacuum environment
demonstrated a high degree of linearity, which further indicates that the heat balance of the
RWT in its flight configuration is conduction-dominated and that radiative factors are
minimal.

With these findings in mind, the original 22-node analytical model used for determination of
aerodynamic heating rates per unit-projected area (A_p) versus altitude was simplified so that
the required program inputs could be limited to tables of external radiative fluxes ($\dot{Q}_{SOLAR}$,
$\dot{Q}_{ALBEDO}$, $\dot{Q}_{IR}$) and RWT temperature (T_W) versus time or altitude. Thus, the simplified
heat balance used to generate aerodynamic heating rate ($\dot{q}_{AERO}$) versus altitude for the eight
selected orbits took the following form:

$$\dot{q}_{AERO} = \frac{K^*}{A_p} (T_W - T^*) - \left[\alpha_s (\dot{Q}_{SOLAR} + \dot{Q}_{ALBEDO}) + \epsilon \dot{Q}_{IR} \right] \tag{16}$$

Although this equation was used to compute a discrete aerodynamic heating rate at each
specified altitude, the final tabulated aerodynamic heating profiles (figures 6 to 13) were
smoothed by application of a least-squares cubic-curve-fit routine to the above collection of
discrete aerodynamic heating rates for each orbit.

15
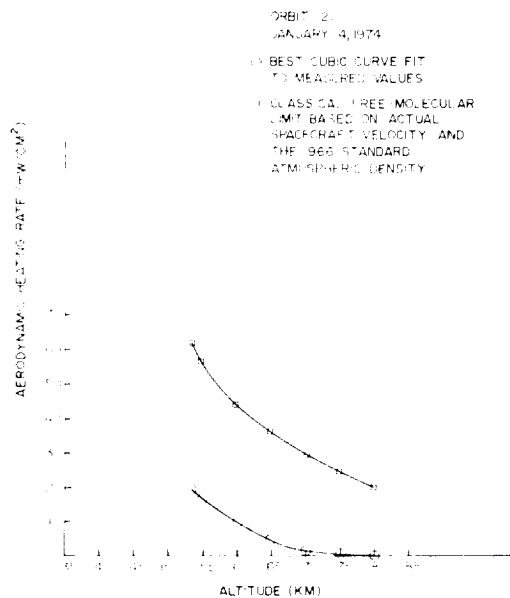
Figure 6. Aerodynamic heating rate versus spacecraft altitude for a fine tungsten wire broadside to the free stream.
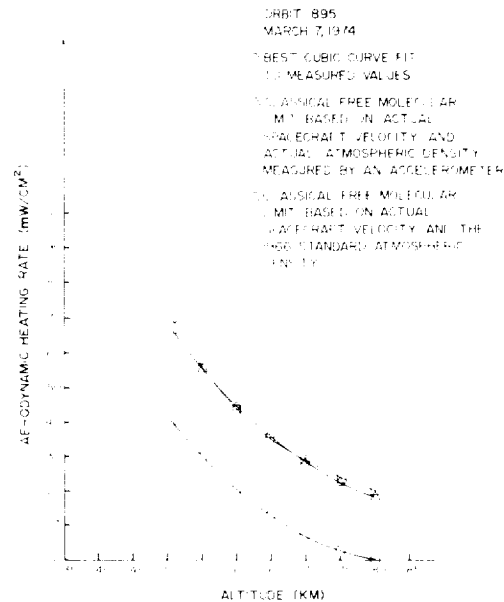
Figure 7. Aerodynamic heating rate versus spacecraft altitude for a fine tungsten wire broadside to the free stream.
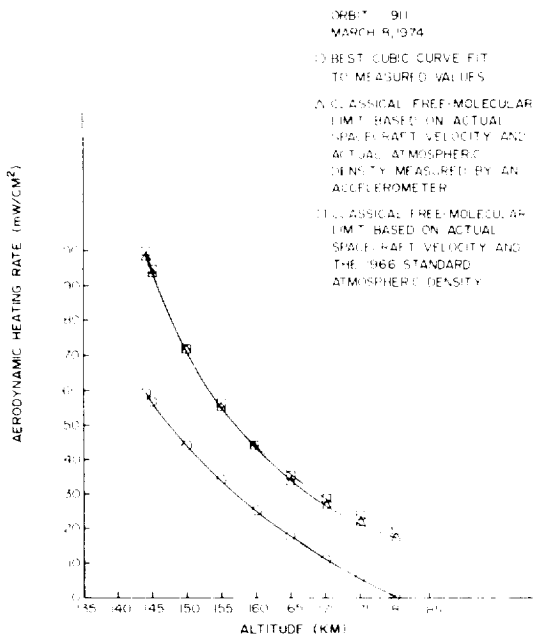
Figure 8. Aerodynamic heating rate versus spacecraft altitude for a fine tungsten wire broadside to the free stream.
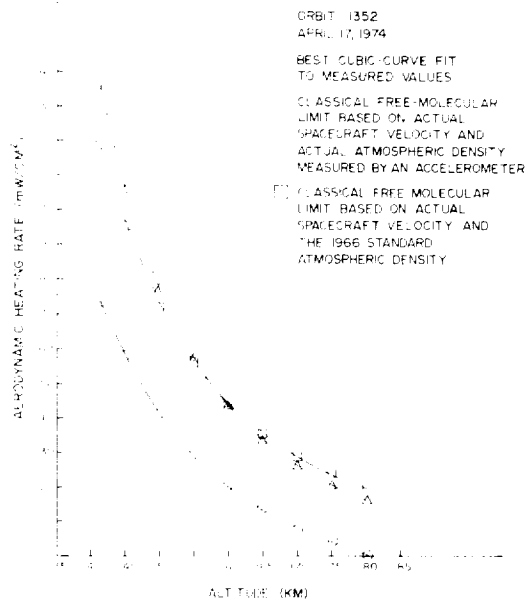
Figure 9. Aerodynamic heating rate versus spacecraft altitude for a fine tungsten wire broadside to the free stream.

16
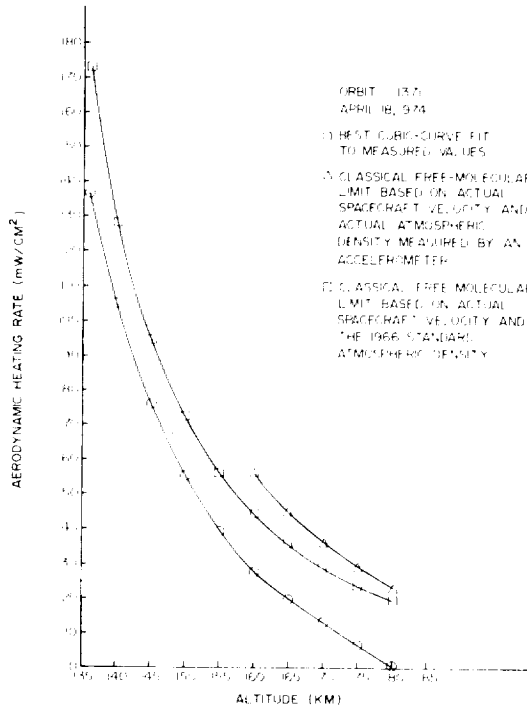
Figure 10. Aerodynamic heating rate versus spacecraft altitude for a fine tungsten wire broadside to the free stream.
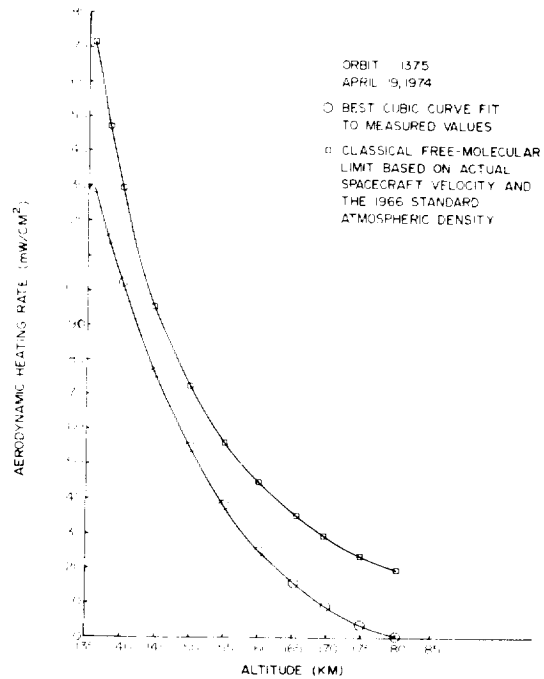
Figure 11. Aerodynamic heating rate versus spacecraft altitude for a fine tungsten wire broadside to the free stream.
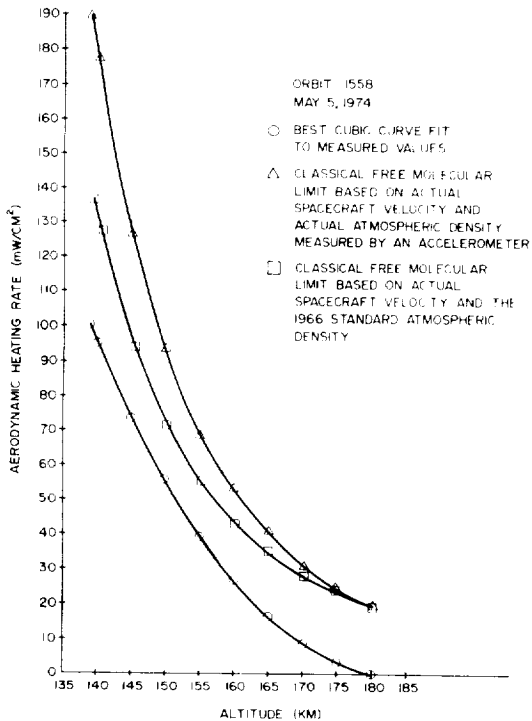
Figure 12. Aerodynamic heating rate versus spacecraft altitude for a fine tungsten wire broadside to the free stream.
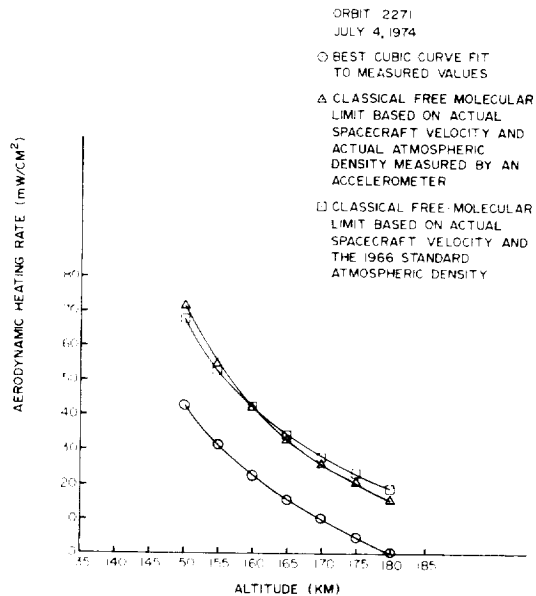
Figure 13. Aerodynamic heating rate versus spacecraft altitude for a fine tungsten wire broadside to the free stream.

17

Estimation of Uncertainties and Errors

The major analytical uncertainty is related to difficulty in specifying the temperature/time response of the RWT support pegs during orbital radiative and/or convective heating. Even though, by careful selection of orbital conditions, the support temperature was known at the onset and conclusion of aerodynamic heating, the precise shape of the temperature/time curve could not readily be determined and was therefore approximated as a straight line connecting the end-point temperatures. The uncertainty attributable to the temperature/time response of the supports is random with the magnitude of uncertainty estimated for a 1-sigma ($\bar{\sigma}$) confidence level from the following equation:

$$\bar{\sigma} = \sqrt{\frac{\sum_{i=1}^{N^*} (\dot{q}_{AERO}^{(1)} - \dot{q}_{AERO}^{(2)})^2}{N^* - 1}} \tag{17}$$

In addition to the foregoing uncertainty, the largest single error is attributable to omission of radiative exchange between the RWT and space and between the RWT and sensor housing. Radiation loss errors ($\dot{q}_{RAD}$) are not random and were conservatively calculated using peak aerodynamic heating conditions. In equation form,

$$-\dot{q}_{RAD} = \frac{\pi}{2} \sigma^* \epsilon \left(T_W^4 - T_{SH}^4 \right) + \frac{\pi}{2} \sigma^* \epsilon \left(T_W^4 - T_{SP}^4 \right) \tag{18}$$

or

$$-\dot{q}_{RAD} = \frac{\pi}{2} \sigma^* \epsilon \left(2T_W^4 - T_{SH}^4 \right) \tag{18a}$$

where σ^* is the Stefan-Boltzmann constant, T_{SH} is the temperature of the sensor housing measured in orbit by a flight thermistor, and T_{SP} is the space background temperature of 0 K.

Other uncertainties and errors have been considered negligible with respect to those specified above. The uncertainties and errors per unit-projected area for the eight selected orbits are given in table 2.

THEORETICAL ORBITAL AERODYNAMIC HEATING RATES

The AE-C spacecraft and TAL-C instrument most probably encounter free-molecular flow conditions in the upper part of the altitude range investigated here (145 to 180 km) with nearly free-molecular flow (first-order collision regime) conditions prevailing toward the lower end of the included altitude range (135.7 to 145 km). Because of the difficulty in

18

Table 2
Uncertainty and Error Estimates

Orbit Number	$\overline{\sigma}$ (mW/cm^2)	$\dot{q}_{RAD\ MAX.}$ (mW/cm^2)	$\dot{q}_{AERO\ MAX.}$ (mW/cm^2)	% Max. Uncertainty	% Max. Error
211	±4.38	-1.58	19.32	±22.67	-8.18
895	±3.63	-2.46	40.16	± 9.04	-6.13
911	±1.99	-5.77	59.46	± 3.35	-9.70
1352	±6.15	-5.36	73.70	± 8.34	-7.27
1371	±8.20	-5.80	136.66	± 6.00	-4.24
1375	±6.02	-4.92	129.31	± 4.66	-3.80
1558	±8.45	-4.29	100.63	± 8.40	-4.26
2271	±5.92	-0.91	42.72	±13.86	-2.13

precisely defining the transition altitude between these two flow regimes, theoretical aerodynamic heating rates were calculated under both free-molecular and near-free-molecular assumptions for the entire altitude range.

Atmospheric density values used in the following mathematical formulas have been determined from drag measurements derived from an accelerometer (MESA) flown on the AE-C spacecraft (F. A. Marcos, unpublished data from the Atmosphere Explorer-C Mission, June 1975) when data were available, and from the 1966 U.S. Standard Atmosphere Supplements (Reference 13).

Finally, the effective accommodation coefficient as a function of altitude was found by taking the ratio of the empirical aerodynamic heating rate to the theoretical free-molecular aerodynamic heating rate for each of the two density assumptions.

Free-Molecular Flow Formulation

On the basis of kinetic theory, the free-molecular heat flux to a surface oriented normal to the free stream is given by

$$
\dot{q}_{FM} = \frac{\overline{\alpha}\rho_\infty \left(\frac{RT_\infty}{M}\right)^{3/2}}{\sqrt{2\pi}} \left\{ \left[S_\infty^2 + \frac{\gamma}{(\gamma-1)} - \frac{(\gamma+1)}{2(\gamma-1)} \frac{T_w}{T_\infty} \right] \right.
$$

$$
\left. \cdot \left[e^{-(S_\infty \sin\theta)^2} + \sqrt{\pi}\, S_\infty \sin\theta \left[1 + erf(S_\infty \sin\theta) \right] \right] - \frac{1}{2} e^{-(S_\infty \sin\theta)^2} \right\}
$$

(19)

19

where

θ is the angle the free-stream velocity vector makes with the surface

and

erf ( ) is the error function defined as

$$erf(\chi) = \frac{2}{\sqrt{\pi}} \int_{0}^{\chi} e^{-\chi^2} d\chi \qquad (20)$$

For application to the TAL-C tungsten RWT, empirical heating rates have been calculated on the basis of the surface projected area; therefore, $\sin \theta$ will be set equal to unity in equation 19. Moreover, because S_∞ is a large value (actually greater than 10 for each orbit selected), the error function of S_∞ approaches the limiting value of 1 (Reference 37), and equation 19 can be simplified to (Reference 38):

$$\dot{q}_{FM} = \bar{\alpha}\rho_\infty \sqrt{2} \left(\frac{RT_\infty}{M}\right)^{3/2} \cdot S_\infty \left[S_\infty^2 + \frac{\gamma}{(\gamma-1)} - \frac{(\gamma+1)}{2(\gamma-1)} \frac{T_W}{T_\infty} \right] \qquad (21)$$

By use of equation 7 and the definition of the free-stream speed ratio (equations 5 and 6), equation 21 can be reduced further to yield

$$\dot{q}_{FM} = \frac{1}{2} \bar{\alpha}\rho_\infty U^3 \left\{ 1 - \frac{(\gamma+1)}{2\gamma} \frac{T_W}{T_O} \right\} \qquad (22)$$

Because $T_W/T_O \sim 0.01$ and $(\gamma + 1)/2\gamma \sim 0.87$ for the orbits selected, the free-molecular-heating rate is given within 1 percent of the previous formulation by the approximation

$$\dot{q}_{FM} \approx \frac{1}{2} \bar{\alpha}\rho_\infty U^3 \qquad (23)$$

Because the accommodation coefficient of atmospheric constituents on tungsten as a function of orbital altitude is not known *a priori*, the free-molecular-heating rates presented in figures 6 to 13 for density values based on the 1966 Standard Atmosphere Supplements ($\dot{q}_{FM\ 1966}$) and for density values based on drag measurements from AE-C ($\dot{q}_{FM\ MESA}$) assume an $\bar{\alpha}$ of unity with the effective accommodation coefficient given by the respective ratios

$$\frac{\dot{q}_{AERO}}{\dot{q}_{FM\ 1966}} \quad \text{and} \quad \frac{\dot{q}_{AERO}}{\dot{q}_{FM\ MESA}}$$

20

Near Free-Molecular Flow Formulation

If the Knudsen number is large but not large enough to ensure the full validity of the free-molecular flow formulation, analysis based upon kinetic theory can still be performed, taking only first-order collisions into account. As previously defined, a first-order collision is one between a free-stream molecule and a reflected or emitted molecule where each molecule is allowed to have one intermolecular collision, but all second or subsequent collisions are neglected (Reference 18).

The near-free-molecular heat flux ($\dot{q}_{NFM}$) to a surface is given in terms of the free-molecular heat flux by the following relationship (References 39 and 40).

$$\frac{\dot{q}_{NFM}}{\dot{q}_{FM}} = \left[1 + 2\left(\frac{T_w}{T_\infty}\right)\frac{1}{S_\infty^2} - 0.1414 S_\infty \left(\frac{T_\infty}{T_w}\right)^{1/2} \frac{1}{Kn_\infty} \right] \tag{24}$$

where the quantity in brackets is denoted as ϕ in the Appendix.

Near-free-molecular heating rates ($\dot{q}_{NFM\ 1966}$ and $\dot{q}_{NFM\ MESA}$) for each selected orbit range from about 97 percent of the free-molecular value at 180 km to about 75 percent of the free-molecular value at 135.7 km.

CORRELATION OF THEORY AND MEASUREMENT BY MEANS OF DIMENSIONLESS GROUPS

Dimensionless groups (Reference 41) provide an invaluable aid in correlation of AE-C flight data with theory and ground test data reported in the literature on cylinders in rarefied high-speed flow.

For convective heat transfer in a rarefied atmosphere, dimensionless groups, such as Nusselt number and Stanton number, are useful for data analysis and correlation. The Nusselt number provides a convenient way of determining the convective heat-transfer coefficient for a body exposed to a gas stream. In mathematical terms,

$$Nu_\infty = \frac{h_\infty D}{k_\infty} \tag{25}$$

where h_∞ is the average convective heat-transfer coefficient based on free-stream conditions, and the other quantities are as previously defined. For a cylinder in hypersonic flow where $Kn_\infty \gg 1$ and $S_\infty > 4$, it has been shown (Reference 42) that the convective heat-transfer coefficient based on free-stream conditions is given by the relation

$$h_\infty = \frac{\overline{\alpha}(\gamma + 1)\rho_\infty C_V U}{2\pi M} \tag{26}$$

21

This equation can be applied equally well to either the AE-C spacecraft or the TAL-C tungsten resistance-wire thermometer if the appropriate $\bar{\alpha}$ is used. Likewise, to calculate Nu_∞, the appropriate characteristic dimension must be selected. Nusselt numbers based on flight data correlate reasonably well with the literature when the effective diameter of the spacecraft is selected as the characteristic dimension.

To compute values of average heat-transfer coefficient (h*) and Nusselt number (Nu*) on the basis of flight results for comparison with theoretical values given by equations 25 and 26, the following relationship was employed

$$\dot{q}_{AERO} A_p = h^*A (T_R - T_W) \qquad (27)$$

Thus,

$$h^* = \frac{\dot{q}_{AERO}}{\pi (T_R - T_W)} \qquad (28)$$

where T_R is the recovery temperature of the body discussed later in this section. Table 3 lists theoretical and flight Nusselt numbers versus altitude for a typical low-perigee orbit (orbit 1371).

Table 3
Theoretical and Empirical Nusselt
Number Versus Altitude

Altitude (km)	Nu_∞ $(\bar{\alpha} = 1)$	Nu*
180.0	0.140	0
175.1	0.164	0.048
170.0	0.205	0.088
165.0	0.254	0.135
160.0	0.317	0.201
155.0	0.408	0.280
150.0	0.539	0.398
145.0	0.723	0.584
140.0	1.011	0.818
135.7	1.419	1.125

Average convective heat-transfer coefficient and Nusselt number are plotted as a function of altitude in figures 14 and 15. In addition, Nusselt number is plotted as a function of Reynolds number in figure 16.
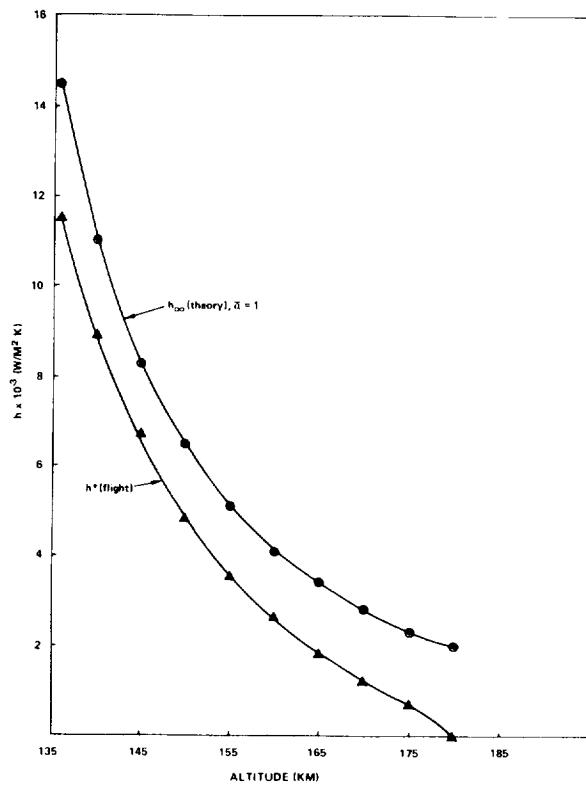
Figure 14. Convective heat-transfer coefficient versus
altitude for a typical low-perigee pass.
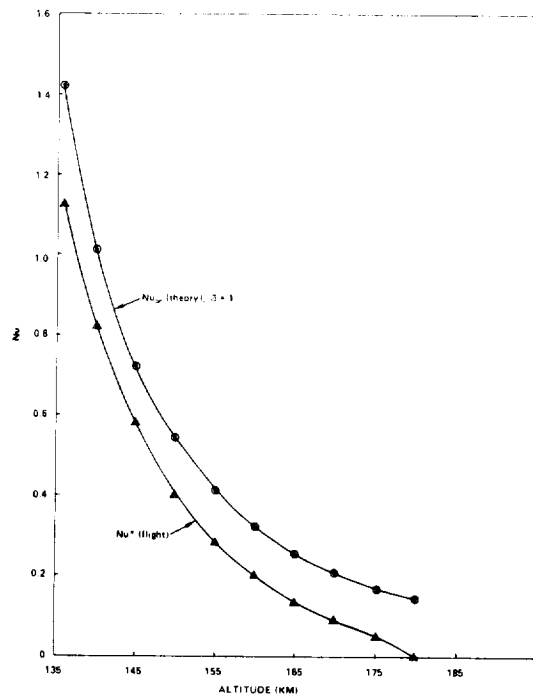
Figure 15. Nusselt number versus altitude
for a typical low-perigee pass.

23
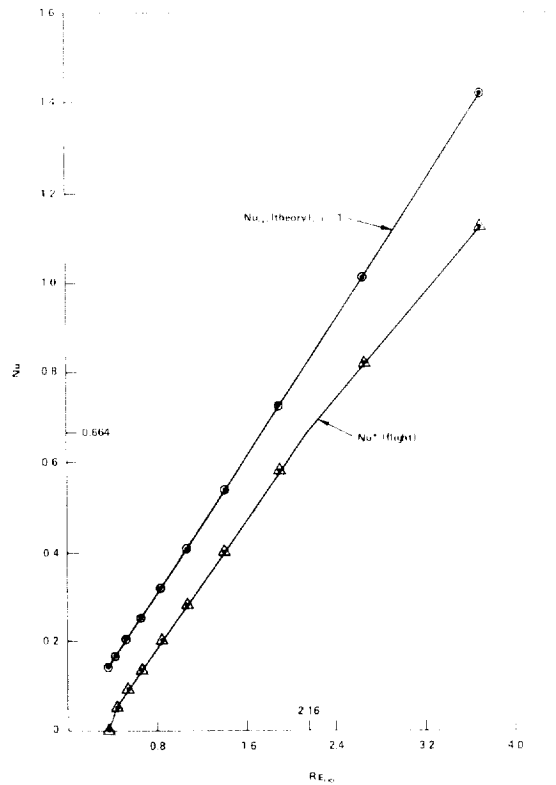
Figure 16. Nusselt number versus Reynolds number
for a typical low-perigee pass.

Figures 14 and 15 show that flight values for the heat-transfer coefficient and Nusselt number are lower than the theoretical values based on an accommodation coefficient of unity. This fact implies that the actual accommodation coefficient for atmospheric gases on tungsten wire is considerably less than 1. The graphs also show that the accommodation coefficient decreases as altitude increases and approaches zero at about 180 km.

When Nusselt number is plotted versus Reynolds number (figure 16), values based on flight data are also lower than those based on free-molecular flow theory. Although absolute magnitudes differ, flight data follow the trends exhibited in the wind-tunnel test data correlation of Reference 43 where supersonic heat transfer from transverse cylinders in rarefied air flow is presented as a function of Reynolds number. The slight kink in the flight Nusselt number versus Reynolds-number curve at $Nu = 0.664$ and $Re_\infty = 2.16$ (figure 16) suggests the possibility that this deviation from a straight-line profile represents a slight change in the character of the flow at an altitude between 140 and 145 km. Such a change in flow regime from free molecular to near-free molecular in the foregoing altitude range is consistent with the conclusions presented earlier.

Another dimensionless group that is useful in forced-convection heat-transfer correlations is the Stanton number. This quantity is equal to the heat transferred to the fluid divided by the heat transported by the fluid (Reference 41). In equation form,

24

$$St_\infty = \frac{h_\infty M}{\rho_\infty C_p U} \tag{29}$$

Table 4 lists theoretical and flight Stanton numbers versus altitude for a typical low-perigee orbit (orbit 1371).

Table 4
Theoretical and Empirical Stanton Number
Versus Altitude

Altitude (km)	St_∞ $(\bar\alpha = 1)$	St^*
180.0	0.280	0
175.1	0.272	0.079
170.0	0.276	0.118
165.0	0.278	0.147
160.0	0.274	0.174
155.0	0.275	0.189
150.0	0.277	0.205
145.0	0.275	0.222
140.0	0.274	0.221
135.7	0.274	0.218

The theoretical free-stream Stanton numbers calculated from equation 29 agree favorably with Oppenheim's formulation for convective heat transfer in free-molecular flow past a transverse cylinder (Reference 37). From Oppenheim,

$$\frac{\gamma}{\bar\alpha(\gamma + 1)} \ St_\infty \cong 0.159 \tag{30}$$

for $S_\infty > 5$. If $\bar\alpha = 1$ and $\gamma = 1.4$, then $St_\infty = 0.273$, and this value compares closely with the theoretical values given in table 4.

Figures 17 and 18 illustrate theoretical and flight Stanton numbers versus altitude and Reynolds number, respectively. Figure 17 illustrates that flight Stanton numbers also imply that the accommodation coefficient for atmospheric gases on tungsten wire is considerably less than 1. Moreover, Stanton number decreases abruptly with increasing altitude because the accommodation coefficient is not constant, but also decreases with altitude. Figure 18 shows that, as Reynolds number increases, flight Stanton number increases until a plateau of about 0.22 is reached for Reynolds numbers greater than about 1.92.

It is advantageous for calculation of heat-transfer rates in rarefied flow to introduce the concepts of recovery temperature and recovery factor. In the absence of heat transfer from a body (adiabatic assumption), the temperature that the body attains is called the recovery

25
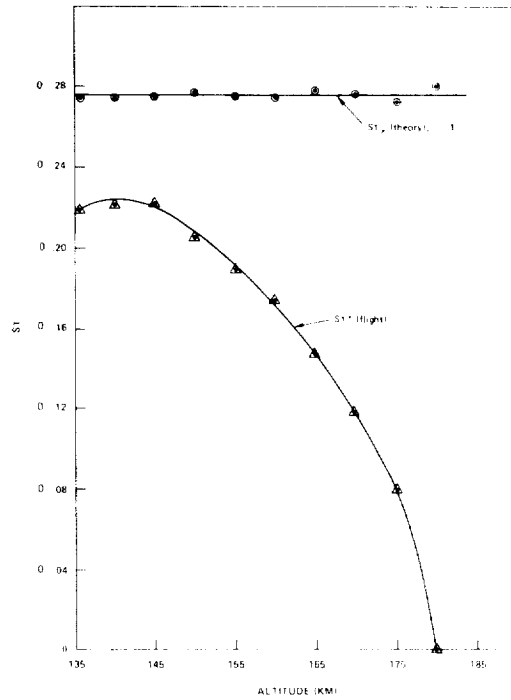
Figure 17. Stanton number versus altitude
for a typical low-perigee pass.
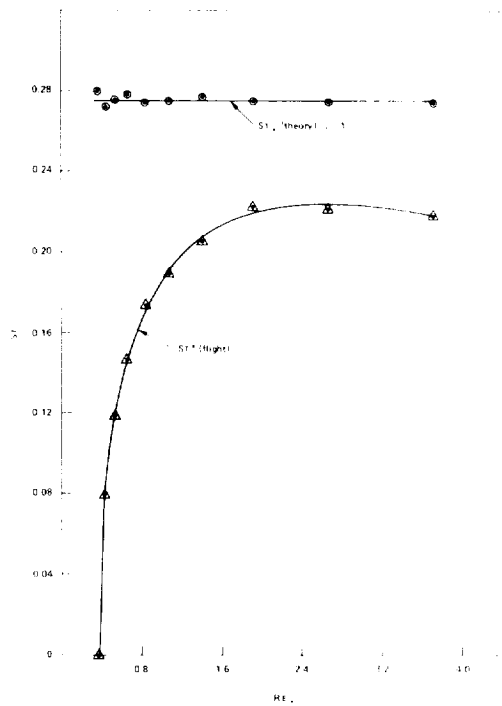
Figure 18. Stanton number versus Reynolds number
for a typical low-perigee pass.

26

temperature. A mathematical expression for the recovery temperature (T_R) can be found by setting $\dot{q} = 0$ in equation 21 with $T_W = T_R$. Therefore,

$$\frac{T_R}{T_\infty} = \frac{2(\gamma - 1)}{(\gamma + 1)} \left[S_\infty^2 + \frac{\gamma}{(\gamma - 1)} \right] \qquad (31)$$

The recovery temperature is therefore different from the stagnation temperature (T_0) given similarly by equation 7:

$$\frac{T_0}{T_\infty} = 1 + \left(\frac{\gamma - 1}{\gamma} \right) S_\infty^2 \qquad (7)$$

Computations presented in the Appendix have shown that $T_R > T_0$ for the eight selected AE-C low-perigee orbits analyzed here. This surprising fact is explained in the literature and has been confirmed by ground tests on insulated cylinders in rarefied flow. Stalder, et al. (Reference 44) point out that, because of the net energy deficiency of the reemitted effusive stream for a given wall temperature, a body in free-molecular flow will attain a temperature higher than that attained in a continuum flow. This phenomenon is in direct contrast to the corresponding phenomenon which occurs under continuum-flow conditions in which an insulated body can have, at most, a temperature equal to the stream total temperature and normally does not even attain this temperature because of the outward flow of heat in the boundary layer.

The recovery temperature and stagnation temperature have been incorporated into a dimensionless group called the recovery factor. The recovery factor (r) is expressed mathematically as

$$r = \frac{T_R - T_\infty}{T_0 - T_\infty} \qquad (32)$$

so that $r < 1$ if $T_R < T_0$, $r = 1$ if $T_R = T_0$, and $r > 1$ if $T_R > T_0$.

The recovery factor for the AE-C spacecraft and TAL-C tungsten wires computed from equations 7, 31, and 32 is approximately 1.16. This value compares favorably with the recovery factor for free-molecular flow past a transverse circular cylinder given by Oppenheim (Reference 37) as

$$\left(\frac{\gamma + 1}{\gamma} \right) r = 2.00 \qquad (33)$$

for $S_\infty > 5$. Thus, if $\gamma = 1.4$ in the above equation, then $r = 1.167$.

Note that all static and dynamic flight parameters introduced in this document have been tabulated as a function of altitude for the eight selected AE-C orbits. These tables are contained in the Appendix.

SUMMARY AND CONCLUSIONS

The Atmosphere Explorer (AE) spacecraft are unique because, by means of an on-board orbit-adjust propulsion system, they are capable of dipping into the sensible portion of the Earth's atmosphere. During such perigee maneuvers, the spacecraft and scientific instruments experience transient aerodynamic heating that is sizable with respect to direct solar, albedo, and earthshine fluxes. Concerns about survival of experiment low-mass tungsten grid wires during these maneuvers and difficulties in analytically modeling such components led to the inclusion of an engineering measurement unit called the Temperature Alarm (TAL). The Temperature Alarm subsystem has been described in detail in previous papers (References 2, 3, and 4).

The AE-C spacecraft on which this document is based has been operated at a spin rate of 4 rpm with perigee heights as low as 130 km and has been despun at 1 rpo for perigee heights as low as 135 km. During the first 6 months of the mission, two perigee lowerings were executed to bring the spacecraft down to 130 km in increments of 5 km. It was during these maneuvers, in both spinning and despun modes for a period of 15 minutes on either side of perigee, that the TAL-C gathered the bulk of engineering data used for aerodynamic heating determination as a function of perigee altitude.

For perigee heights between 155 km and 130 km, flight-temperature measurements (Reference 4) indicate that orbital aerodynamic heating of low thermal mass elements results in temperature extremes substantially lower than those predicted. For example, at an altitude of 130 km, a conservative preflight prediction for the peak temperature of a tungsten resistance-wire thermometer exposed to aerodynamic heating only was about 573 K. Actual in-flight measurements were of the order of 373 K. The maximum temperature experienced to date on a tungsten resistance-wire thermometer has been approximately 423 K, and this case included aerodynamic heating at 135 km in the despun mode, as well as a sizable energy contribution from direct solar at perigee. Temperature predictions have been judged to be ultraconservative because analytical treatment of conductive coupling and contact resistance is intractable for fine-wire elements wrapped around more massive supports; therefore, conservative assumptions were made in the analyses. Moreover, conservative classical free-molecular heating rates, in which the accommodation coefficient of atmospheric constituents on tungsten is assumed to be unity, were employed in thermal analyses because flight data in this regime are not available.

Much effort has been expended to generate an acceptable thermal mathematical model for the TAL-C tungsten resistance-wire thermometer. Analytical work has shown that the heat balance of a fine tungsten wire wrapped around more massive, low conductivity support pegs

28

is conduction-dominated. Consequently, the sensitive parameters in the analysis relate to the conductive heat transfer between the wire grids and the support pegs, as well as to the solar absorptivity of tungsten wire. The conductive coupling was estimated from analysis of selected orbital data, and the solar absorptivity of fine tungsten wire and the thermal capacitance of a support peg were determined by ground testing. With this information in hand, the analytical model used for determination of aerodynamic heating rates versus altitude was simplified so that required program inputs could be limited to tables of external radiative fluxes and resistance-wire thermometer temperatures versus time or altitude. Therefore, based on in-flight orbital temperature data from the TAL-C, aerodynamic heating rates (figures 6 to 13) have been determined for eight selected orbits by means of a reduced thermal analytical model verified by both ground test and flight data. These heating rates are compared with the classical free-molecular values.

It has been concluded that, for engineering purposes, the aerodynamic heating rate of atmospheric gases at perigee altitudes between 170 and 135 km on pure tungsten wire is 25 to 60 percent of the value set by the classical free-molecular limit where MESA flight densities were used in the computations. Such low values for the accommodation coefficient of tungsten during orbital flight give credence to the trends that are reported in Reference 32 through 35 and discussed in this document.

At higher altitudes, the aerodynamic heating rate decreases further and becomes negligible at altitudes above 182 km. Relative to the more usual orbital thermal input attributable to direct solar radiation, the aerodynamic heating rate at the lowest altitude attempted with the spacecraft despun (135 km) is the equivalent of about 1.2 solar constants incident on a tungsten wire with a solar absorptivity of 0.85.

Correlation of Nusselt and Stanton numbers based on flight data with those from free-molecular flow theory indicates that flight values are considerably lower than the theoretical limiting values based on perfect accommodation ($\bar{\alpha} = 1$). Even though absolute magnitudes may differ, flight data follow the trends expected when Nusselt and Stanton numbers are presented as a function of altitude or Reynolds number.

ACKNOWLEDGMENTS

REFERENCES

1. *Radio Science,* 8 (4), April 1973.

2. Young, Earle W., "The Atmosphere Explorer-C Spacecraft Temperature Alarm," (Proceedings of the Institute of Environmental Sciences), April 28 to May 1, 1974, pp. 147-151.

3. Caruso, Paul S., Jr., "Heat Flux Calibration of a Near Earth Spacecraft Temperature Alarm System in Rarefied Flow," (Proceedings of the Institute of Environmental Sciences), April 28 to May 1, 1974, pp. 170-175.

4. Young, Earle W., Jr., and Paul S. Caruso, Jr., "A Satellite Temperature-Flux Monitor For Low Perigee Applications," (Proceedings of the Instrument Society of America, ISA ASI 75225), May 19 to 21, 1975, pp. 133-143.

5. *Entry Gasdynamic Heating,* NASA SP-8062, January 1971.

6. Stalder, Jackson R., Glen Goodwin, and Marcus O. Creager, *Heat Transfer to Bodies in a High-Speed Rarefied-Gas Stream,* NACA TN 2438, Washington, D.C., August 1951.

7. Matting, Fred W., "Approximate Bridging Relations in the Transitional Regime between Continuum and Free-Molecule Flows," *Journal of Spacecraft,* 8 (1), January 1971, pp. 35-40.

8. Vogenitz, F. W., G. A. Bird, J. E. Broadwell, and H. Rungaldier, "Theoretical and Experimental Study of Rarefied Supersonic Flows about Several Simple Shapes," *AIAA Journal,* 6 (12), December 1968, pp. 2388-2394.

9. Rochelle, W. C., B. B. Roberts, F. W. Vogenitz, and L. d'Attorre, "Space Shuttle Orbiter Reentry Flow Field and Heating Analysis," NASA TM X-2506, Space Shuttle Aerothermodynamics Technology Conference (Vol. I-Flow Fields), Washington, D.C., February 1972, pp. 115-156.

10. Pirello, C. J., R. D. Hardin, M. V. Heckart, and K. R. Brown, *An Inventory of Aeronautical Ground Research Facilities,* NASA CR-1874, Vol. 1 - Wind Tunnels, Washington, D.C., November 1971.

11. The 1959 ARDC Model Atmosphere, AFCRC-TR-59-267, Air Force Cambridge Research Center, Cambridge, Massachusetts, 1959.

12. *U.S. Standard Atmosphere*, 1962. U.S. Government Printing Office, 1962.

13. *U.S. Standard Atmosphere Supplements*, 1966. U.S. Government Printing Office, 1966.

14. *Models of Earth's Atmosphere (120 to 1000 km)*, NASA SP-8021, May 1969.

15. Jacchia, L. G., "Recent Advances in Upper Atmosphere Structure," *Space Research X*, North Holland Publishing Company, Amsterdam, 1970, pp. 367-388.

16. Champion, K. S. W., F. A. Marcos, and R. A. Schweinfurth, "Measurements by the Low Altitude Density Satellite OV1-16," *Space Research X*, North Holland Publishing Company, Amsterdam, 1970, pp. 459-466.

17. Sears, Francis Weston, "An Introduction to Thermodynamics," *The Kinetic Theory of Gases, and Statistical Mechanics* (Second Edition), Addison-Wesley Publishing Company, Inc., Reading, Massachusetts, 1953.

18. Hayes, Wallace D., and Ronald F. Probstein, *Hypersonic Flow Theory*, Academic Press, New York, 1959.

19. Lam, L. S., G. M. Mendes, and C. A. Lundquist, *Design of Satellite Experiment for Atmospheric Density and Near-Free-Molecule-Flow Aerodynamics*, SAO Special Report 241, Smithsonian Institution Astrophysical Observatory, Cambridge, Massachusetts, June 5, 1967.

20. Whitfield, David L., *Drag on Bodies in Rarefied High-Speed Flow*, dissertation, University of Tennessee, Nashville, December 1971.

21. Wuest, W. and G. Koppenwallner, "The Hypersonic Low Density Wind-Tunnel of the Aerodynamische Versuchsanstalt Goettingen Operational Behavior and Results on Vibrational Relaxation," AIAA Paper No. 68-49, *AIAA 6th Aerospace Sciences Meeting*, New York, January 22 to 24, 1968.

22. Klett, Robert D., *Drag Coefficients and Heating Ratios for Right Circular Cylinders in Free-Molecular and Continuum Flow from Mach 10 to 30*, SC-RR-64-2141, Sandia Laboratory, Albuquerque, New Mexico, December 1964.

23. Vincenti, Walter G., and Charles H. Kruger, Jr., *Introduction to Physical Gas Dynamics*, John Wiley and Sons, Inc., New York, 1965.

24. Hartnett, J. P., "A Survey of Thermal Accommodation Coefficients," *Rarefied Gas Dynamics*, Supplement 1, L. Talbot, Ed., Academic Press, New York, 1961, pp. 1-28.

25. Cook, G. E., "Satellite Drag Coefficients," *Planetary and Space Science*, 13, May 1965, pp. 929-946.

26. Klett, D. E., and R. K. Irey, "Methods for Determining Thermal Accommodation Coefficients From Free Molecule Flow Heat Transfer, " (Proceedings of Space, Technology, and Society, Vol. 1), Canaveral Council of Technical Societies, 6th Space Congress, Cocoa Beach, Florida, March 17 to 19, 1969, pp. 1-1 to 1-8.

27. Knechtel, Earl D., and William C. Pitts, "Normal and Tangential Momentum Accommodation for Earth Satellite Conditions," *Astronautica Acta*, 18, June 1973, pp. 171-184.

28. Hurlbut, F. C., and F. S. Sherman, "Application of the Nocilla Wall Reflection Model to Free-Molecule Kinetic Theory," *Physics of Fluids*, 11 (3), March 1968, pp. 486-496.

29. Bird, G. A., "The Free-Molecule Flow Field of a Moving Body in the Upper Atmosphere," *Rarefied Gas Dynamics*, Supplement 1, L. Talbot, (Ed.), Academic Press, New York, 1961, pp. 245-259.

30. Datz, S., G. E. Moore, and E. H. Taylor, "The Reflection of Modulated Helium and Deuterium Molecular Beams From Platinum Surfaces," *Rarefied Gas Dynamics*, Supplement 2, J. A. Laurmann, (Ed.), Academic Press, New York, 1963, pp. 347-361.

31. Hyson, Peter, "The Tungsten Wire Temperature Sensor," *Journal of Applied Meteorology*, 7, August 1968, pp. 684-690.

32. Eckert, E. R. G., and R. M. Drake, *Heat and Mass Transfer*, McGraw Hill, New York, 1959.

33. Cybulski, R. J., and L. V. Baldwin, *Heat Transfer from Cylinders in Transition From Slip Flow to Free Molecule Flow*, NASA Memo 4-27-59E, 1959.

34. Roberts, J. K., "The Exchange of Energy between Gas Atoms and Solid Surfaces," (Proceedings of the Royal Society), Series A, 129, July 1930, pp. 146-161.

35. Roberts, J. K., "The Exchange of Energy between Gas Atoms and Solid Surfaces, II-The Temperature Variation of the Accommodation Coefficient of Helium," (Proceedings of the Royal Society), Series A, 135, February/April 1932, pp. 192-205.

36. Powers, E. I., *Thermal Radiation to a Flat Surface Rotating About an Arbitrary Axis in an Elliptical Earth Orbit: Application to Spin-Stabilized Satellites*, NASA TN-D-2147, NASA Langley Research Center, Virginia, April 1964.

37. Oppenheim, A. K., "Generalized Theory of Convective Heat Transfer in a Free-Molecule Flow," *Journal of the Aeronautical Sciences*, January 1953, pp. 49-58.

38. Whitfield, David L., *Rarefied Flow Heat-Flux Calibration of an Earth Satellite Temperature Alarm System,* LTR-AEDC-VKF-ASP-1-73, Arnold Air Force Station, Tennessee, March 1973.

39. *Aerodynamic Heating on the SSS-A Spacecraft,* (Final Report to NASA/GSFC under contract NAS5-11800), AVCO Government Products Group, AVCO Systems Division, Wilmington, Massachusetts, February 16, 1971.

40. Hammerling, P., and B. Kivel, "Heat Transfer to a Sphere at the Transition from Free Molecular Flow, *Physics of Fluids,* 1 (4), July/August 1958.

41. Land, Norman S., *A Compilation of Nondimensional Numbers,* NASA SP-274, Washington, D.C., 1972.

42. Lord, P. G., "Hot-Wire Probe End-Loss Corrections in Low Density Flows," *Journal of Physics E: Scientific Instruments,* 7, January 1974, pp. 56-60.

43. Baldwin, Lionel V., Virgil A. Sandborn, and James C. Laurence, "Heat Transfer From Transverse and Yawed Cylinders in Continuum, Slip, and Free Molecule Air Flows," *Transactions of the ASME, Series C, Journal of Heat Transfer,* May 1960, pp. 77-86.

44. Stalder, Jackson R., Glen Goodwin, and Marcus O. Creager, *A Comparison of Theory and Experiment for High Speed Free-Molecule Flow,* NACA TN-2244, Washington, D.C., December 1950.

34

APPENDIX

STATIC AND DYNAMIC FLIGHT PARAMETERS
FOR EIGHT SELECTED ORBITS

Table 1

Static and Dynamic Flight Parameters for Orbit 211

Altitude (km)	ρ_∞ (kg/m³)	T_∞ (K)	M (kg/kgmole)	λ_∞ (m)	Kn_∞	U (m/s)	C_{mp} (m/s)	S_∞	T_o/T_∞	S_o	λ_o (m)	Kn_o	$\bar{V}$ (m/s)
179.4	6.334×10^{-10}	878.6	23.84	105.57	77.62	8666	782.9	11.07	32.77	1.93	71.88	52.85	883.1
175.1	7.406×10^{-10}	862.8	24.05	91.08	66.97	8675	772.4	11.23	33.70	1.93	62.02	45.60	871.3
170.1	8.975×10^{-10}	842.2	24.29	75.91	55.82	8676	759.4	11.42	35.52	1.92	51.86	38.13	856.6
165.0	1.104×10^{-9}	817.9	24.53	62.33	45.83	8675	744.6	11.65	36.93	1.92	42.59	31.32	839.9
160.1	1.365×10^{-9}	790.9	24.77	50.90	37.43	8682	728.7	11.91	38.55	1.92	34.78	25.57	822.0
155.0	1.725×10^{-9}	758.8	25.01	40.67	29.90	8692	710.3	12.24	41.46	1.90	27.97	20.57	801.2
153.4	1.870×10^{-9}	747.4	25.09	37.64	27.68	8693	703.8	12.35	42.19	1.90	25.89	19.04	793.9
155.0	1.725×10^{-9}	758.8	25.01	40.67	29.90	8693	710.3	12.24	41.46	1.90	27.97	20.57	801.2
160.1	1.365×10^{-9}	790.9	24.77	50.90	37.43	8682	728.7	11.91	38.55	1.92	34.78	25.57	822.0
165.1	1.099×10^{-9}	818.3	24.53	62.60	46.03	8676	744.8	11.65	36.93	1.92	42.77	31.45	840.1
170.2	8.944×10^{-10}	842.7	24.28	76.16	56.00	8670	759.7	11.41	35.46	1.92	52.03	38.26	856.9
175.0	7.427×10^{-10}	862.5	24.05	90.84	66.79	8671	772.2	11.23	33.70	1.93	61.86	45.49	871.0
180.0	6.180×10^{-10}	880.5	23.81	108.08	79.47	8664	784.2	11.05	32.66	1.93	73.59	54.11	884.6

(Rows 1–7 labeled DOWNLEG; rows 8–13 labeled UPLEG)

Table 1 (Continued)

Altitude (km)	ν_∞ (m²/s)	$R_{E\infty}$	C_v/R	C_p/R	γ	k_∞ (W/m K)	h^* (W/m² K)	h_∞/α (W/m² K)	T_R/T_∞	r	T_w/T_∞	T_w/T_o
179.4	31076.3	0.38	2.83	3.83	1.35	0.0194	0	0.0020	37.65	1.15	0.28	0.0085
175.1	26452.7	0.45	2.82	3.82	1.35	0.0191	0	0.0023	38.71	1.15	0.28	0.0083
170.1	21674.8	0.54	2.80	3.80	1.36	0.0186	0.00013	0.0028	40.94	1.16	0.29	0.0082
165.0	17450.3	0.68	2.78	3.78	1.36	0.0182	0.00044	0.0034	42.56	1.16	0.30	0.0081
160.1	13946.6	0.85	2.76	3.76	1.36	0.0176	0.00089	0.0041	44.43	1.16	0.31	0.0080
155.0	10861.6	1.09	2.73	3.73	1.37	0.0170	0.0015	0.0051	47.93	1.16	0.33	0.0080
153.4	9960.8	1.19	2.72	3.72	1.37	0.0168	0.0017	0.0055	48.78	1.16	0.35	0.0083
155.0	10861.6	1.09	2.73	3.73	1.37	0.0170	0.0015	0.0051	47.93	1.16	0.34	0.0082
160.1	13946.6	0.85	2.76	3.76	1.36	0.0176	0.00089	0.0041	44.43	1.16	0.33	0.0086
165.1	17530.1	0.67	2.78	3.78	1.36	0.0182	0.00043	0.0034	42.56	1.16	0.32	0.0087
170.2	21753.8	0.54	2.80	3.80	1.36	0.0187	0.00013	0.0028	40.87	1.16	0.31	0.0087
175.0	26373.9	0.45	2.82	3.82	1.35	0.0191	0	0.0023	38.71	1.15	0.30	0.0089
180.0	31869.2	0.37	2.83	3.83	1.35	0.0195	0	0.0020	37.52	1.15	0.29	0.0089

(Row groups: DOWNLEG for altitudes 179.4–153.4; UPLEG for altitudes 155.0–180.0)

Table 1 (Continued)

Altitude (km)	$\dot{q}_{SOLAR}$ (mW/cm^2)	$\dot{q}_{ALBEDO}$ (mW/cm^2)	$\dot{q}_{IR}$ (mW/cm^2)	$\dot{q}_{AERO}$ (mW/cm^2)	$\dot{q}_{FM\ 1966}$ (mW/cm^2)	$\dot{q}_{FM\ MESA}$ (mW/cm^2)	$\dot{q}_{NFM\ 1966}$ (mW/cm^2)	$\dot{q}_{NFM\ MESA}$ (mW/cm^2)	$\dfrac{\dot{q}_{AERO}}{\dot{q}_{FM\ 1966}}$	$\dfrac{\dot{q}_{AERO}}{\dot{q}_{FM\ MESA}}$	$\dfrac{\dot{q}_{AERO}}{\dot{q}_{NFM\ 1966}}$	$\dfrac{\dot{q}_{AERO}}{\dot{q}_{NFM\ MESA}}$	ϕ
179.4	0	0	0.193	0	20.61		19.91		0		0		0.966
175.1	0	0	0.194	0	24.17		23.20		0		0		0.960
170.1	0	0	0.196	1.45	29.31	Not Available For This Orbit	27.87	Not Available For This Orbit	0.05	Not Available For This Orbit	0.05	Not Available For This Orbit	0.951
165.0	0	0	0.197	4.79	36.04		33.84		0.13		0.14		0.939
160.1	0	0	0.198	9.74	44.66		41.27		0.22		0.24		0.924
155.0	0	0	0.200	16.74	56.64		51.20		0.30		0.33		0.904
153.4	0	0	0.200	19.32	61.42		55.16		0.31		0.35		0.898
155.0	0	0	0.200	16.74	56.66		51.28		0.30		0.33		0.905
160.1	0	0	0.199	9.74	44.66		41.36		0.22		0.24		0.926
165.1	0	0	0.198	4.70	35.89		33.77		0.13		0.14		0.941
170.2	0	0	0.197	1.39	29.14		27.77		0.05		0.05		0.953
175.0	0	0	0.196	0	24.21		23.27		0		0		0.961
180.0	0	0	0.196	0	20.10		19.46		0		0		0.968

(Rows 179.4–153.4: DOWNLEG; rows 155.0–180.0: UPLEG)

39

Table 2

Static and Dynamic Flight Parameters for Orbit 895

Altitude (km)	ρ_∞ (kg/m^3)	T_∞ (K)	M (kg/kgmole)	λ_∞ (m)	Kn_∞	U (m/s)	C_{mp} (m/s)	S_∞	T_o/T_∞	S_o	λ_o (m)	Kn_o	$\overline{V}$ (m/s)
179.9	6.206×10^{-10}	880.2	23.81	107.64	79.15	8627	784.0	11.00	32.37	1.93	73.29	53.89	884.4
175.0	7.427×10^{-10}	862.5	24.05	90.84	66.79	8634	772.2	11.18	33.41	1.93	61.85	45.48	871.0
169.9	9.045×10^{-10}	841.2	24.29	75.35	55.40	8636	758.8	11.38	35.28	1.92	51.48	37.85	855.9
164.9	1.109×10^{-9}	817.3	24.53	62.06	45.63	8641	744.3	11.61	36.68	1.92	42.40	31.18	839.6
160.1	1.365×10^{-9}	790.9	24.77	50.90	37.43	8644	728.7	11.86	38.23	1.92	34.78	25.57	822.0
155.0	1.725×10^{-9}	758.8	25.01	40.67	29.90	8653	710.3	12.18	41.07	1.90	27.97	20.57	801.2
150.7	2.150×10^{-9}	727.6	25.23	32.92	24.21	8658	692.5	12.50	43.20	1.90	22.64	16.65	781.1
155.0	1.725×10^{-9}	758.8	25.01	40.67	29.90	8646	710.3	12.17	41.00	1.90	27.97	20.57	801.2
160.0	1.369×10^{-9}	790.4	24.77	50.76	37.32	8646	728.4	11.87	38.30	1.92	34.68	25.50	821.6
164.9	1.109×10^{-9}	817.3	24.53	62.06	45.63	8635	744.3	11.60	36.62	1.92	42.40	31.18	839.6
170.0	9.006×10^{-10}	841.8	24.29	75.66	55.63	8630	759.1	11.37	35.22	1.92	51.69	38.01	856.3
175.1	7.406×10^{-10}	862.8	24.05	91.08	66.97	8628	772.4	11.17	33.35	1.93	62.02	45.60	871.3
180.1	6.164×10^{-10}	880.8	23.81	108.34	79.66	8624	784.4	10.99	32.31	1.93	73.76	54.24	884.8

Table 2 (Continued)

Altitude (km)	ν_∞ (m²/s)	$R_{E\infty}$	C_v/R	C_p/R	γ	k_∞ (W/m K)	h^* (W/m² K)	h_∞/α (W/m² K)	T_R/T_∞	r	T_W/T_∞	T_W/T_o
179.9	31732.3	0.37	2.83	3.83	1.35	0.0195	0	0.0020	37.19	1.15	0.35	0.0108
175.0	26373.9	0.45	2.82	3.82	1.35	0.0191	0.00027	0.0023	38.38	1.15	0.37	0.0111
169.9	21497.4	0.55	2.80	3.80	1.36	0.0186	0.00067	0.0028	40.66	1.16	0.38	0.0108
164.9	17368.5	0.68	2.78	3.78	1.36	0.0181	0.0012	0.0034	42.28	1.16	0.40	0.0109
160.1	13946.6	0.84	2.76	3.76	1.36	0.0176	0.0019	0.0041	44.07	1.16	0.42	0.0110
155.0	10861.6	1.08	2.73	3.73	1.37	0.0170	0.0027	0.0051	47.48	1.16	0.45	0.0110
150.7	8571.3	1.37	2.71	3.71	1.37	0.0165	0.0036	0.0063	49.94	1.16	0.49	0.0113
155.0	10861.6	1.08	2.73	3.73	1.37	0.0170	0.0027	0.0051	47.40	1.16	0.47	0.0115
160.0	13901.5	0.85	2.76	3.76	1.36	0.0176	0.0019	0.0041	44.14	1.16	0.45	0.0117
164.9	17368.5	0.68	2.78	3.78	1.36	0.0181	0.0012	0.0034	42.20	1.16	0.44	0.0120
170.0	21595.9	0.54	2.80	3.80	1.36	0.0186	0.00066	0.0028	40.59	1.16	0.42	0.0119
175.1	26452.7	0.44	2.82	3.82	1.35	0.0191	0.00027	0.0023	38.31	1.15	0.41	0.0123
180.1	31953.1	0.37	2.83	3.83	1.35	0.0195	0	0.0020	37.13	1.15	0.40	0.0124

(Left row labels: rows 2–8 marked DOWNLEG; rows 9–13 marked UPLEG)

Table 2 (Continued)

Altitude (km)	$\dot{q}_{SOLAR}$ (mW/cm²)	$\dot{q}_{ALBEDO}$ (mW/cm²)	$\dot{q}_{IR}$ (mW/cm²)	$\dot{q}_{AERO}$ (mW/cm²)	$\dot{q}_{FM\ 1966}$ (mW/cm²)	$\dot{q}_{FM\ MESA}$ (mW/cm²)	$\dot{q}_{NFM\ 1966}$ (mW/cm²)	$\dot{q}_{NFM\ MESA}$ (mW/cm²)	$\dfrac{\dot{q}_{AERO}}{\dot{q}_{FM\ 1966}}$	$\dfrac{\dot{q}_{AERO}}{\dot{q}_{FM\ MESA}}$	$\dfrac{\dot{q}_{AERO}}{\dot{q}_{NFM\ 1966}}$	$\dfrac{\dot{q}_{AERO}}{\dot{q}_{NFM\ MESA}}$	ϕ
179.9	99.74	0.070	0.196	0	19.92	17.40	19.38	16.93	0	0	0	0	0.973
175.0	99.95	0.088	0.197	2.80	23.90	21.82	23.11	21.10	0.12	0.13	0.12	0.13	0.967
169.9	100.14	0.166	0.198	7.12	29.13	27.60	27.94	26.47	0.24	0.26	0.25	0.27	0.959
164.9	100.19	0.356	0.198	12.89	35.78	36.13	33.96	34.29	0.36	0.36	0.38	0.38	0.949
160.1	100.26	0.584	0.199	20.18	44.08	42.95	41.30	40.24	0.46	0.47	0.49	0.50	0.937
155.0	100.21	0.981	0.200	29.98	55.88	53.77	51.41	49.47	0.54	0.56	0.58	0.61	0.920
150.7	99.75	1.88	0.201	40.16	69.77	66.52	62.93	60.00	0.58	0.60	0.64	0.67	0.902
155.0	98.13	3.12	0.200	29.98	55.74	57.20	51.39	52.74	0.54	0.52	0.58	0.57	0.922
160.0	97.08	3.59	0.199	20.33	44.24	46.21	41.54	43.39	0.46	0.44	0.49	0.47	0.939
164.9	96.48	3.94	0.198	12.89	35.70	37.34	33.99	35.55	0.36	0.34	0.38	0.36	0.952
170.0	95.72	4.22	0.196	7.03	28.94	29.56	27.84	28.44	0.24	0.24	0.25	0.25	0.962
175.1	95.01	4.46	0.195	2.74	23.78	23.25	23.07	22.55	0.12	0.12	0.12	0.12	0.970
180.1	94.38	4.67	0.194	0	19.77	18.28	19.30	17.84	0	0	0	0	0.976

Table 3

Static and Dynamic Flight Parameters for Orbit 911

Altitude (km)	ρ_∞ (kg/m³)	T_∞ (K)	M (kg/kgmole)	λ_∞ (m)	Kn_∞	U (m/s)	C_{mp} (m/s)	S_∞	T_o/T_∞	S_o	λ_o (m)	Kn_o	$\bar{V}$ (m/s)
180.0	6.180×10^{-10}	880.5	23.81	108.08	79.47	8622	784.2	10.99	32.31	1.93	73.59	54.11	884.6
174.9	7.462×10^{-10}	862.0	24.05	90.43	66.49	8622	771.9	11.17	33.35	1.93	61.58	45.28	870.7
170.1	8.975×10^{-10}	842.2	24.29	75.91	55.82	8632	759.4	11.37	35.22	1.92	51.86	38.13	856.6
164.9	1.109×10^{-9}	817.3	24.53	62.06	45.63	8635	744.3	11.60	36.62	1.92	42.40	31.18	839.6
160.0	1.369×10^{-9}	790.4	24.77	50.76	37.32	8645	728.4	11.87	38.30	1.92	34.68	25.50	821.6
154.9	1.732×10^{-9}	758.0	25.02	40.52	29.79	8653	709.8	12.19	41.13	1.90	27.87	20.49	800.7
150.0	2.214×10^{-9}	722.4	25.26	32.01	23.54	8654	689.6	12.55	43.54	1.90	22.02	16.19	777.9
145.0	2.910×10^{-9}	680.5	25.51	24.59	18.08	8658	666.0	13.00	46.64	1.90	16.92	12.44	751.2
144.1	3.080×10^{-9}	670.8	25.55	23.27	17.11	8657	660.7	13.10	47.35	1.90	16.01	11.77	745.3
145.0	2.910×10^{-9}	680.5	25.51	24.59	18.08	8655	666.0	13.00	46.64	1.90	16.92	12.44	751.2
150.0	2.214×10^{-9}	722.4	25.26	32.01	23.54	8653	689.6	12.55	43.54	1.90	22.02	16.19	777.9
154.9	1.732×10^{-9}	758.0	25.02	40.52	29.79	8650	709.8	12.19	41.13	1.92	27.87	20.49	800.7
160.0	1.369×10^{-9}	790.4	24.77	50.76	37.32	8642	728.4	11.86	38.23	1.92	34.68	25.50	821.6
165.0	1.104×10^{-9}	817.9	24.53	62.33	45.83	8640	744.6	11.60	36.62	1.92	42.58	31.31	839.9
169.9	9.045×10^{-10}	841.2	24.29	75.35	55.40	8629	758.8	11.37	35.22	1.92	51.48	37.85	855.9
175.0	7.427×10^{-10}	862.5	24.05	90.84	66.79	8626	772.2	11.17	33.35	1.93	61.85	45.48	871.0
180.2	6.148×10^{-10}	881.1	23.80	108.60	79.85	8613	784.6	10.98	32.26	1.93	73.94	54.37	885.0

(Rows in the upper group labelled DOWNLEG; rows in the lower group labelled UPLEG.)

Table 3 (Continued)

Altitude (km)	ν_∞ (m²/s)	R_{E_∞}	C_v/R	C_p/R	γ	k_∞ (W/m K)	h^* (W/m² K)	$h_\infty/\bar{\alpha}$ (W/m² K)	T_R/T_∞	r	T_w/T_∞	T_w/T_o
180.0	31869.2	0.37	2.83	3.83	1.35	0.0195	0.00005	0.0020	37.13	1.15	0.34	0.0105
174.9	26245.8	0.45	2.82	3.82	1.35	0.0191	0.00056	0.0023	38.31	1.15	0.35	0.0105
170.1	21674.8	0.54	2.80	3.80	1.36	0.0186	0.0010	0.0028	40.59	1.16	0.36	0.0102
164.9	17368.5	0.68	2.78	3.78	1.36	0.0181	0.0017	0.0034	42.20	1.16	0.38	0.0104
160.0	13901.5	0.85	2.76	3.76	1.36	0.0176	0.0023	0.0041	44.14	1.16	0.40	0.0104
154.9	10814.8	1.09	2.73	3.73	1.37	0.0170	0.0030	0.0051	47.55	1.16	0.43	0.0105
150.0	8300.2	1.42	2.71	3.71	1.37	0.0164	0.0039	0.0064	50.33	1.16	0.46	0.0106
145.0	6157.3	1.91	2.67	3.67	1.37	0.0156	0.0050	0.0083	53.92	1.16	0.51	0.0109
144.1	5781.0	2.04	2.67	3.67	1.37	0.0155	0.0052	0.0087	54.74	1.16	0.53	0.0112
145.0	6157.3	1.91	2.67	3.67	1.37	0.0156	0.0050	0.0083	53.92	1.16	0.53	0.0114
150.0	8300.2	1.42	2.71	3.71	1.37	0.0164	0.0039	0.0064	50.33	1.16	0.50	0.0115
154.9	10814.8	1.09	2.73	3.73	1.37	0.0170	0.0030	0.0051	47.55	1.16	0.47	0.0114
160.0	13901.5	0.85	2.76	3.76	1.36	0.0176	0.0023	0.0041	44.07	1.16	0.45	0.0118
165.0	17450.3	0.67	2.78	3.78	1.36	0.0182	0.0016	0.0034	42.20	1.16	0.44	0.0120
169.9	21497.4	0.55	2.80	3.80	1.36	0.0186	0.0011	0.0028	40.59	1.16	0.43	0.0122
175.0	26373.9	0.44	2.82	3.82	1.35	0.0191	0.00055	0.0023	38.31	1.15	0.41	0.0123
180.2	32037.0	0.37	2.83	3.83	1.35	0.0195	0.00003	0.0020	37.06	1.15	0.40	0.0124

Table 3 (Continued)

Altitude (km)	$\dot{q}_{SOLAR}$ (mW/cm²)	$\dot{q}_{ALBEDO}$ (mW/cm²)	$\dot{q}_{IR}$ (mW/cm²)	$\dot{q}_{AERO}$ (mW/cm²)	$\dot{q}_{FM\ 1966}$ (mW/cm²)	$\dot{q}_{FM\ MESA}$ (mW/cm²)	$\dot{q}_{NFM\ 1966}$ (mW/cm²)	$\dot{q}_{NFM\ MESA}$ (mW/cm²)	$\dfrac{\dot{q}_{AERO}}{\dot{q}_{FM\ 1966}}$	$\dfrac{\dot{q}_{AERO}}{\dot{q}_{FM\ MESA}}$	$\dfrac{\dot{q}_{AERO}}{\dot{q}_{NFM\ 1966}}$	$\dfrac{\dot{q}_{AERO}}{\dot{q}_{NFM\ MESA}}$	ϕ
180.0	94.61	0.005	0.196	0.50	19.81	17.08	19.26	16.60	0.03	0.03	0.03	0.03	0.972
174.9	94.91	0.011	0.197	5.74	23.91	21.22	23.07	20.48	0.24	0.27	0.25	0.28	0.965
170.1	95.21	0.013	0.198	11.10	28.86	26.43	27.65	25.32	0.38	0.42	0.40	0.44	0.958
164.9	95.59	0.019	0.199	17.72	35.70	33.48	33.81	31.71	0.50	0.53	0.52	0.56	0.947
160.0	95.78	0.059	0.200	25.03	44.22	42.64	41.35	39.87	0.56	0.59	0.61	0.63	0.935
154.9	96.02	0.110	0.200	34.08	56.11	54.75	51.51	50.26	0.61	0.62	0.66	0.68	0.918
150.0	96.30	0.169	0.202	44.42	71.75	72.26	64.22	64.67	0.62	0.61	0.69	0.69	0.895
145.0	96.29	0.764	0.202	56.96	94.43	94.76	81.59	81.87	0.60	0.60	0.70	0.70	0.864
144.1	96.28	1.04	0.202	59.46	99.91	98.29	85.62	84.23	0.60	0.60	0.69	0.71	0.857
145.0	95.83	1.68	0.202	56.96	94.33	92.71	81.78	80.38	0.60	0.61	0.70	0.71	0.867
150.0	95.11	2.40	0.201	44.42	71.72	71.27	64.55	64.14	0.62	0.62	0.69	0.69	0.900
154.9	94.52	2.81	0.200	34.08	56.05	55.66	51.68	51.32	0.61	0.61	0.66	0.66	0.922
160.0	94.03	3.15	0.199	25.03	44.18	43.24	41.48	40.60	0.57	0.58	0.60	0.62	0.939
165.0	93.43	3.41	0.198	17.59	35.60	34.18	33.93	32.57	0.49	0.51	0.52	0.54	0.953
169.9	92.95	3.62	0.198	11.34	29.06	27.31	27.96	26.27	0.39	0.42	0.41	0.43	0.962
175.0	92.46	3.83	0.197	5.63	23.84	21.82	23.12	21.17	0.24	0.26	0.24	0.27	0.970
180.2	91.95	4.05	0.194	0.32	19.64	17.54	19.17	17.12	0.02	0.02	0.02	0.02	0.976

(Left margin markers: DOWN LEG for descending altitudes; UP LEG for ascending altitudes.)

Table 4

Static and Dynamic Flight Parameters for Orbit 1352

Altitude (km)	ρ_∞ (kg/m³)	T_∞ (K)	M (kg/kgmole)	λ_∞ (m)	Kn_∞	U (m/s)	C_{mp} (m/s)	S_∞	T_o/T_∞	S_o	λ_o (m)	Kn_o	$\overline{V}$ (m/s)
180.1	6.164×10^{-10}	880.8	23.81	108.34	79.66	8637	784.4	11.01	32.43	1.93	73.76	54.24	884.8
175.1	7.406×10^{-10}	862.8	24.05	91.08	66.97	8645	772.4	11.19	33.46	1.93	62.02	45.60	871.3
170.0	9.006×10^{-10}	841.8	24.29	75.66	55.63	8650	759.1	11.40	35.40	1.92	51.69	38.01	856.3
165.0	1.104×10^{-9}	817.9	24.53	62.33	45.83	8654	744.6	11.62	36.74	1.92	42.58	31.31	839.9
159.9	1.374×10^{-9}	789.7	24.77	50.58	37.19	8663	728.0	11.90	38.48	1.92	34.56	25.41	821.2
155.0	1.725×10^{-9}	758.8	25.01	40.67	29.90	8664	710.3	12.20	41.20	1.90	27.97	20.57	801.2
150.0	2.214×10^{-9}	722.4	25.26	32.01	23.54	8668	689.6	12.57	43.67	1.90	22.02	16.19	777.9
145.0	2.910×10^{-9}	680.5	25.51	24.59	18.08	8677	666.0	13.03	46.85	1.90	16.92	12.44	751.2
141.3	3.630×10^{-9}	643.0	25.70	19.86	14.60	8681	645.0	13.46	50.89	1.89	13.71	10.08	727.6
145.0	2.910×10^{-9}	680.5	25.51	24.59	18.08	8681	666.0	13.03	46.85	1.90	16.92	12.44	751.2
150.0	2.214×10^{-9}	722.4	25.26	32.01	23.54	8671	689.6	12.57	43.67	1.90	22.02	16.19	777.9
154.9	1.732×10^{-9}	758.0	25.02	40.52	29.79	8668	709.8	12.21	41.26	1.90	27.87	20.49	800.7
159.8	1.380×10^{-9}	789.0	24.78	50.37	37.04	8663	727.7	11.90	38.48	1.92	34.42	25.31	820.8
164.9	1.109×10^{-9}	817.3	24.53	62.06	45.63	8657	744.3	11.63	36.80	1.92	42.40	31.18	839.6
170.2	8.944×10^{-10}	842.7	24.28	76.16	56.00	8645	759.7	11.38	35.28	1.92	52.03	38.26	856.9
175.2	7.384×10^{-10}	863.1	24.04	91.34	67.16	8643	772.6	11.19	33.46	1.93	62.20	45.74	871.5
180.3	6.132×10^{-10}	881.4	23.80	108.87	80.05	8644	784.8	11.01	32.43	1.93	74.12	54.50	885.3

(First group: DOWNLEG; second group: UPLEG)

46

Table 4 (Continued)

Altitude (km)	ν_∞ (m²/s)	$R_{E\infty}$	C_v/R	C_p/R	γ	k_∞ (W/m K)	h^* (W/m² K)	$h_\infty/\bar{\alpha}$ (W/m² K)	T_R/T_∞	r	T_w/T_∞	T_w/T_o
180.1	31953.1	0.37	2.83	3.83	1.35	0.0195	0.000070	0.0020	37.26	1.15	0.29	0.0089
175.1	26452.7	0.44	2.82	3.82	1.35	0.0191	0.00043	0.0023	38.45	1.15	0.30	0.0090
170.0	21595.9	0.54	2.80	3.80	1.36	0.0186	0.00078	0.0028	40.80	1.16	0.31	0.0088
165.0	17450.3	0.67	2.78	3.78	1.36	0.0182	0.0012	0.0034	42.35	1.16	0.32	0.0087
159.9	13845.4	0.85	2.76	3.76	1.36	0.0176	0.0018	0.0041	44.36	1.16	0.34	0.0088
155.0	10861.6	1.08	2.73	3.73	1.37	0.0170	0.0026	0.0051	47.63	1.16	0.36	0.0087
150.0	8300.2	1.42	2.71	3.71	1.37	0.0164	0.0037	0.0065	50.49	1.16	0.38	0.0087
145.0	6157.3	1.92	2.67	3.67	1.37	0.0156	0.0051	0.0083	54.17	1.16	0.42	0.0090
141.3	4816.7	2.45	2.64	3.64	1.38	0.0149	0.0062	0.0102	59.01	1.16	0.47	0.0092
145.0	6157.3	1.92	2.67	3.67	1.37	0.0156	0.0051	0.0083	54.17	1.16	0.44	0.0094
150.0	8300.2	1.42	2.71	3.71	1.37	0.0164	0.0037	0.0065	50.49	1.16	0.41	0.0094
154.9	10814.8	1.09	2.73	3.73	1.37	0.0170	0.0026	0.0051	47.71	1.16	0.39	0.0095
159.8	13781.2	0.85	2.76	3.76	1.36	0.0176	0.0018	0.0042	44.36	1.16	0.37	0.0096
164.9	17368.5	0.68	2.78	3.78	1.36	0.0181	0.0012	0.0034	42.42	1.16	0.35	0.0095
170.2	21753.8	0.54	2.80	3.80	1.36	0.0187	0.00076	0.0028	40.66	1.16	0.34	0.0096
175.2	26534.3	0.44	2.82	3.82	1.35	0.0191	0.00042	0.0023	38.45	1.15	0.33	0.0099
180.3	32127.5	0.37	2.83	3.83	1.35	0.0195	0.000056	0.0020	37.26	1.15	0.32	0.0099

(Row groups labeled "DOWNLEG" for altitudes 170.0–150.0 and "UPLEG" for altitudes 154.9–170.2.)

Table 4 (Continued)

Altitude (km)	$\dot{q}_{SOLAR}$ (mW/cm²)	$\dot{q}_{ALBEDO}$ (mW/cm²)	$\dot{q}_{IR}$ (mW/cm²)	$\dot{q}_{AERO}$ (mW/cm²)	$\dot{q}_{FM\ 1966}$ (mW/cm²)	$\dot{q}_{FM\ MESA}$ (mW/cm²)	$\dot{q}_{NFM\ 1966}$ (mW/cm²)	$\dot{q}_{NFM\ MESA}$ (mW/cm²)	$\dfrac{\dot{q}_{AERO}}{\dot{q}_{FM\ 1966}}$	$\dfrac{\dot{q}_{AERO}}{\dot{q}_{FM\ MESA}}$	$\dfrac{\dot{q}_{ALERO}}{\dot{q}_{NFM\ 1966}}$	$\dfrac{\dot{q}_{AERO}}{\dot{q}_{NFM\ MESA}}$	ϕ
180.1	0	0.673	0.195	0.72	19.86	16.33	19.22	15.81	0.04	0.04	0.04	0.05	0.968
175.1	0	0.552	0.196	4.41	23.92	20.42	23.01	19.64	0.18	0.22	0.19	0.22	0.962
170.0	0	0.423	0.197	8.35	29.14	26.12	27.77	24.89	0.29	0.32	0.30	0.34	0.953
165.0	0	0.284	0.198	13.18	35.78	33.70	33.67	31.71	0.37	0.39	0.39	0.42	0.941
159.9	0	0.129	0.199	19.96	44.66	43.88	41.40	40.68	0.45	0.45	0.48	0.49	0.927
155.0	0	0.088	0.200	29.00	56.09	57.88	50.99	52.61	0.52	0.50	0.57	0.55	0.909
150.0	0	0.046	0.201	41.52	72.09	77.50	63.58	68.36	0.58	0.54	0.65	0.61	0.882
145.0	0	0.003	0.202	58.23	95.05	105.18	80.60	89.19	0.61	0.55	0.72	0.65	0.848
141.3	0	0	0.203	73.70	118.74	135.75	96.77	110.64	0.62	0.54	0.76	0.67	0.815
145.0	0	0	0.202	58.23	95.19	106.63	81.10	90.85	0.61	0.55	0.72	0.64	0.852
150.0	0	0	0.201	41.52	72.17	76.60	64.01	67.94	0.58	0.54	0.65	0.61	0.887
154.9	0	0	0.200	29.19	56.40	56.66	51.44	51.67	0.52	0.52	0.57	0.56	0.912
159.8	0	0	0.199	20.11	44.86	42.58	41.76	39.64	0.45	0.47	0.48	0.51	0.931
164.9	0	0	0.198	13.30	35.98	32.44	33.97	30.62	0.37	0.41	0.39	0.43	0.944
170.2	0	0	0.197	8.16	28.89	25.04	27.62	23.94	0.28	0.32	0.30	0.34	0.956
175.2	0	0	0.196	4.35	23.84	19.95	22.98	19.23	0.18	0.22	0.19	0.23	0.964
180.3	0	0	0.195	0.57	19.80	16.11	19.23	15.64	0.03	0.04	0.03	0.04	0.971

48

Table 5

Static and Dynamic Flight Parameters for Orbit 1371

Altitude (km)	ρ_∞ (kg/m³)	T_∞ (K)	M (kg/kgmole)	λ_∞ (m)	Kn_∞	U (m/s)	C_{mp} (m/s)	S_∞	T_o/T_∞	S_o	λ_o (m)	Kn_o	$\overline{V}$ (m/s)
180.0	6.180×10^{-10}	880.5	23.81	108.08	79.47	8629	784.2	11.00	32.37	1.93	73.59	54.11	884.6
175.1	7.406×10^{-10}	862.8	24.05	91.08	66.97	8644	772.4	11.19	33.46	1.93	62.02	45.60	871.3
170.0	9.006×10^{-10}	841.8	24.29	75.66	55.63	8646	759.1	11.39	35.34	1.92	51.69	38.01	856.3
164.9	1.109×10^{-9}	817.3	24.53	62.06	45.63	8656	744.3	11.63	36.80	1.92	42.40	31.18	839.6
160.0	1.369×10^{-9}	790.4	24.77	50.76	37.32	8655	728.4	11.88	38.36	1.92	34.68	25.50	821.6
154.9	1.732×10^{-9}	758.0	25.02	40.52	29.79	8661	709.8	12.20	41.20	1.90	27.87	20.49	800.7
149.9	2.227×10^{-9}	721.5	25.27	31.83	23.40	8665	689.1	12.57	43.67	1.90	21.89	16.10	777.3
145.0	2.910×10^{-9}	680.5	25.51	24.59	18.08	8674	666.0	13.02	46.78	1.90	16.92	12.44	751.2
140.0	3.943×10^{-9}	632.3	25.76	18.33	13.48	8680	638.9	13.59	51.86	1.89	12.65	9.30	720.7
135.7	5.285×10^{-9}	584.4	25.99	13.79	10.14	8681	611.5	14.20	56.52	1.89	9.52	7.00	689.8
140.0	3.943×10^{-9}	632.3	25.76	18.33	13.48	8674	638.9	13.58	51.78	1.89	12.65	9.30	720.7
145.1	2.895×10^{-9}	681.2	25.51	24.72	18.18	8678	666.4	13.02	46.78	1.90	17.00	12.50	751.7
150.0	2.214×10^{-9}	722.4	25.26	32.01	23.54	8668	689.6	12.57	43.67	1.90	22.02	16.19	777.9
155.0	1.725×10^{-9}	758.8	25.01	40.67	29.90	8657	710.3	12.19	41.13	1.90	27.97	20.57	801.2
160.1	1.365×10^{-9}	790.9	24.77	50.90	37.43	8654	728.7	11.88	38.36	1.92	34.78	25.57	822.0
165.0	1.104×10^{-9}	817.9	24.53	62.33	45.83	8650	744.6	11.62	36.74	1.92	42.59	31.32	839.9
170.1	8.975×10^{-10}	842.2	24.29	75.91	55.82	8643	759.4	11.38	35.28	1.92	51.86	38.13	856.6
175.2	7.384×10^{-10}	863.1	24.04	91.34	67.16	8637	772.6	11.18	33.41	1.93	62.19	45.73	871.5
180.2	6.148×10^{-10}	881.1	23.80	108.60	79.85	8633	784.6	11.00	32.37	1.93	73.94	54.37	885.0

Table 5 (Continued)

Altitude (km)	ν_∞ (m²/s)	R_{E_∞}	C_v/R	C_p/R	γ	k_∞ (W/m K)	h^* (W/m² K)	$h_\infty/\bar{\alpha}$ (W/m² K)	T_R/T_∞	r	T_W/T_∞	T_W/T_o
180.0	31869.2	0.37	2.83	3.83	1.35	0.0195	0	0.0020	37.19	1.15	0.30	0.0093
175.1	26452.7	0.44	2.82	3.82	1.35	0.0191	0.00067	0.0023	38.45	1.15	0.31	0.0093
170.0	21595.9	0.54	2.80	3.80	1.36	0.0186	0.0013	0.0028	40.73	1.16	0.33	0.0093
164.9	17368.5	0.68	2.78	3.78	1.36	0.0181	0.0019	0.0034	42.42	1.16	0.34	0.0092
160.0	13901.5	0.85	2.76	3.76	1.36	0.0176	0.0026	0.0041	44.21	1.16	0.35	0.0091
154.9	10814.8	1.09	2.73	3.73	1.37	0.0170	0.0035	0.0051	47.63	1.16	0.38	0.0092
149.9	8247.2	1.43	2.70	3.70	1.37	0.0163	0.0049	0.0065	50.49	1.16	0.41	0.0094
145.0	6157.3	1.92	2.67	3.67	1.37	0.0156	0.0067	0.0083	54.09	1.16	0.45	0.0096
140.0	4403.5	2.68	2.64	3.64	1.38	0.0148	0.0089	0.0110	60.14	1.16	0.52	0.0100
135.7	3170.8	3.72	2.60	3.60	1.38	0.0139	0.0115	0.0145	65.55	1.16	0.60	0.0106
140.0	4403.5	2.68	2.64	3.64	1.38	0.0148	0.0089	0.0110	60.05	1.16	0.54	0.0104
145.1	6194.0	1.91	2.67	3.67	1.37	0.0156	0.0066	0.0082	54.09	1.16	0.49	0.0105
150.0	8300.2	1.42	2.71	3.71	1.37	0.0164	0.0048	0.0065	50.49	1.16	0.45	0.0103
155.0	10861.6	1.08	2.73	3.73	1.37	0.0170	0.0035	0.0051	47.55	1.16	0.42	0.0102
160.1	13946.6	0.84	2.76	3.76	1.36	0.0176	0.0026	0.0041	44.21	1.16	0.40	0.0104
165.0	17450.3	0.67	2.78	3.78	1.36	0.0182	0.0018	0.0034	42.35	1.16	0.38	0.0103
170.1	21674.8	0.54	2.80	3.80	1.36	0.0186	0.0012	0.0028	40.66	1.16	0.37	0.0105
175.2	26534.3	0.44	2.82	3.82	1.35	0.0191	0.00066	0.0023	38.38	1.15	0.35	0.0105
180.2	32037.0	0.37	2.83	3.83	1.35	0.0195	0	0.0020	37.19	1.15	0.34	0.0105

(Row labels along left margin: DOWNLEG for upper block, UPLEG for lower block)

Table 5 (continued)

Altitude (km)	$\dot{q}_{SOLAR}$ (mW/cm²)	$\dot{q}_{ALBEDO}$ (mW/cm²)	$\dot{q}_{IR}$ (mW/cm²)	$\dot{q}_{AERO}$ (mW/cm²)	$\dot{q}_{FM\,1966}$ (mW/cm²)	$\dot{q}_{FM\,MESA}$ (mW/cm²)	$\dot{q}_{NFM\,1966}$ (mW/cm²)	$\dot{q}_{NFM\,MESA}$ (mW/cm²)	$\dfrac{\dot{q}_{AERO}}{\dot{q}_{FM\,1966}}$	$\dfrac{\dot{q}_{AERO}}{\dot{q}_{FM\,MESA}}$	$\dfrac{\dot{q}_{AERO}}{\dot{q}_{NFM\,1966}}$	$\dfrac{\dot{q}_{AERO}}{\dot{q}_{NFM\,MESA}}$	ϕ
180.0	0	1.47	0.195	0	19.85		19.23		0		0		0.969
175.1	0	1.33	0.196	6.97	23.92		23.03		0.29		0.30		0.963
170.0	0	1.17	0.197	13.37	29.10	Data	27.79	Data	0.46	Data	0.48	Data	0.955
164.9	0	0.992	0.198	20.05	35.96	Not	33.91	Not	0.56	Not	0.59	Not	0.943
160.0	0	0.807	0.199	28.12	44.38	Available	41.23	Available	0.63	Available	0.68	Available	0.929
154.9	0	0.600	0.200	39.66	56.26	For	51.35	For	0.70	For	0.77	For	0.911
149.9	0	0.429	0.201	55.42	72.44	This	64.25	This	0.76	This	0.86	This	0.887
145.0	0	0.249	0.202	76.54	94.96	Orbit	81.10	Orbit	0.81	Orbit	0.94	Orbit	0.854
140.0	0	0.021	0.203	105.23	128.93		104.18		0.82		1.01*		0.808
135.7	0	0	0.204	136.66	172.87		129.65		0.79		1.05*		0.750
140.0	0	0	0.203	105.23	128.66		104.47		0.82		1.01*		0.812
145.1	0	0	0.202	76.04	94.60		81.45		0.80		0.93		0.861
150.0	0	0	0.201	55.07	72.09		64.38		0.76		0.86		0.893
155.0	0	0	0.200	39.37	55.96		51.32		0.70		0.77		0.917
160.1	0	0	0.199	27.93	44.23	56.06	41.36	52.42	0.63	0.50	0.68	0.53	0.935
165.0	0	0	0.198	19.92	35.73	44.98	33.84	42.60	0.56	0.44	0.59	0.47	0.947
170.1	0	0	0.197	13.24	28.97	36.16	27.75	34.64	0.46	0.37	0.48	0.38	0.958
175.2	0	0	0.196	6.84	23.79	29.06	22.98	28.07	0.29	0.24	0.30	0.24	0.966
180.2	0	0	0.195	0	19.78	23.61	19.23	22.95	0	0	0	0	0.972

*Indicates that density from the 1966 Standard Atmosphere is inadequate for this orbit. Density from MESA instrument shows that actual density is greater than 1966 value.

Table 6

Static and Dynamic Flight Parameters for Orbit 1375

Altitude (km)	ρ_∞ (kg/m³)	T_∞ (K)	M (kg/kgmole)	λ_∞ (m)	Kn_∞	U (m/s)	C_{mp} (m/s)	S_∞	T_o/T_∞	S_o	λ_o (m)	Kn_o	$\overline{V}$ (m/s)
180.0	6.180×10^{-10}	880.5	23.81	108.08	79.47	8629	784.2	11.00	32.37	1.93	73.59	54.11	884.6
175.0	7.427×10^{-10}	862.5	24.05	90.84	66.79	8644	772.2	11.19	33.46	1.93	61.85	45.48	871.0
169.9	9.045×10^{-10}	841.2	24.29	75.35	55.40	8644	758.8	11.39	35.34	1.92	51.48	37.85	855.9
165.2	1.094×10^{-9}	818.7	24.52	62.88	46.24	8646	745.1	11.60	36.62	1.92	42.96	31.59	840.5
160.2	1.361×10^{-9}	791.4	24.76	51.04	37.53	8653	729.0	11.87	38.30	1.92	34.88	25.65	822.3
155.0	1.725×10^{-9}	758.8	25.01	40.67	29.90	8658	710.3	12.19	41.13	1.90	27.97	20.57	801.2
150.0	2.214×10^{-9}	722.4	25.26	32.01	23.54	8664	689.6	12.56	43.60	1.90	22.02	16.19	777.9
144.9	2.930×10^{-9}	679.2	25.51	24.43	17.96	8671	665.3	13.03	46.85	1.90	16.81	12.36	750.5
140.0	3.943×10^{-9}	632.3	25.76	18.33	13.48	8675	638.9	13.58	51.78	1.89	12.65	9.30	720.7
138.0	4.500×10^{-9}	609.0	25.87	16.13	11.86	8682	625.7	13.88	54.05	1.89	11.13	8.18	705.8
135.8	5.250×10^{-9}	585.6	25.98	13.88	10.21	8680	612.2	14.18	56.37	1.89	9.58	7.04	690.6
135.9	5.215×10^{-9}	586.8	25.98	13.97	10.27	8682	612.9	14.17	56.29	1.89	9.64	7.09	691.4
138.0	4.500×10^{-9}	609.0	25.87	16.13	11.86	8677	625.7	13.87	53.97	1.89	11.13	8.18	705.8
140.0	3.943×10^{-9}	632.3	25.76	18.33	13.48	8678	638.9	13.58	51.78	1.89	12.65	9.30	720.7
145.0	2.910×10^{-9}	680.5	25.51	24.59	18.08	8671	666.0	13.02	46.78	1.90	16.92	12.44	751.2
150.1	2.207×10^{-9}	723.1	25.26	32.10	23.60	8669	690.0	12.56	43.60	1.90	22.08	16.24	778.3
154.8	1.740×10^{-9}	757.3	25.02	40.34	29.66	8655	709.4	12.20	41.20	1.90	27.74	20.40	800.2
159.9	1.374×10^{-9}	789.7	24.77	50.58	37.19	8656	728.0	11.89	38.42	1.92	34.56	25.41	821.2
164.9	1.109×10^{-9}	817.3	24.53	62.06	45.63	8647	744.3	11.62	36.74	1.92	42.40	31.18	839.6
170.0	9.006×10^{-10}	841.8	24.29	75.66	55.63	8647	759.1	11.39	35.34	1.92	51.69	38.01	856.3
175.1	7.406×10^{-10}	862.8	24.05	91.08	66.97	8642	772.4	11.19	33.46	1.93	62.02	45.60	871.3
180.1	6.164×10^{-10}	880.8	23.81	108.34	79.66	8628	784.4	11.00	32.37	1.93	73.76	54.24	884.8

(Left margin labels: DOWNLEG — upper rows; UPLEG — lower rows)

52

Table 6 (Continued)

Altitude (km)	ν_∞ (m²/s)	$R_{E\infty}$	C_v/R	C_p/R	γ	k_∞ (W/m K)	h^* (W/m² K)	$h_\infty/\bar{\alpha}$ (W/m² K)	T_R/T_∞	r	T_w/T_∞	T_w/T_o
—												
180.0	31869.2	0.37	2.83	3.83	1.35	0.0195	0	0.0020	37.19	1.15	0.30	0.0093
175.0	26373.9	0.45	2.82	3.82	1.35	0.0191	0.00037	0.0023	38.45	1.15	0.31	0.0093
169.9	21497.4	0.55	2.80	3.80	1.36	0.0186	0.00086	0.0028	40.73	1.16	0.32	0.0091
165.2	17616.9	0.67	2.78	3.78	1.36	0.0182	0.0015	0.0033	42.20	1.16	0.34	0.0093
160.2	13990.1	0.84	2.76	3.76	1.36	0.0176	0.0023	0.0041	44.14	1.16	0.36	0.0094
155.0	10861.6	1.08	2.73	3.73	1.37	0.0170	0.0034	0.0051	47.55	1.16	0.38	0.0092
150.0	8300.2	1.42	2.71	3.71	1.37	0.0164	0.0048	0.0065	50.41	1.16	0.41	0.0094
144.9	6111.6	1.93	2.67	3.67	1.37	0.0156	0.0066	0.0083	54.17	1.16	0.45	0.0096
140.0	4403.5	2.68	2.64	3.64	1.38	0.0148	0.0087	0.0110	60.05	1.16	0.52	0.0100
138.0	3794.9	3.11	2.62	3.62	1.38	0.0144	0.0096	0.0125	62.68	1.16	0.55	0.0102
135.8	3195.2	3.69	2.60	3.60	1.38	0.0140	0.0108	0.0144	65.37	1.16	0.59	0.0105
—												
135.9	3219.6	3.67	2.60	3.60	1.38	0.0140	0.0108	0.0143	65.28	1.16	0.60	0.0107
138.0	3794.9	3.11	2.62	3.62	1.38	0.0144	0.0097	0.0125	62.59	1.16	0.56	0.0104
140.0	4403.5	2.68	2.64	3.64	1.38	0.0148	0.0087	0.0110	60.05	1.16	0.53	0.0102
145.0	6157.3	1.92	2.67	3.67	1.37	0.0156	0.0066	0.0083	54.09	1.16	0.49	0.0105
150.1	8327.8	1.42	2.71	3.71	1.37	0.0164	0.0048	0.0064	50.41	1.16	0.45	0.0103
154.8	10760.0	1.09	2.73	3.73	1.37	0.0170	0.0034	0.0052	47.63	1.16	0.42	0.0102
159.9	13845.4	0.85	2.76	3.76	1.36	0.0176	0.0024	0.0041	44.28	1.16	0.40	0.0104
164.9	17368.5	0.68	2.78	3.78	1.36	0.0181	0.0015	0.0034	42.35	1.16	0.38	0.0103
170.0	21595.9	0.54	2.80	3.80	1.36	0.0186	0.00084	0.0028	40.73	1.16	0.37	0.0105
175.1	26452.7	0.44	2.82	3.82	1.35	0.0191	0.00036	0.0023	38.45	1.15	0.35	0.0105
180.1	31953.1	0.37	2.83	3.83	1.35	0.0195	0	0.0020	37.19	1.15	0.34	0.0105
—												

(Left margin labels: DOWNLEG applies to the upper block; UPLEG applies to the lower block.)

Table 6 (continued)

Altitude (km)	$\dot{q}_{SOLAR}$ (mW/cm²)	$\dot{q}_{ALBEDO}$ (mW/cm²)	$\dot{q}_{IR}$ (mW/cm²)	$\dot{q}_{AERO}$ (mW/cm²)	$\dot{q}_{FM\ 1966}$ (mW/cm²)	$\dot{q}_{FM\ MESA}$ (mW/cm²)	$\dot{q}_{NFM\ 1966}$ (mW/cm²)	$\dot{q}_{NFM\ MESA}$ (mW/cm²)	$\dfrac{\dot{q}_{AERO}}{\dot{q}_{FM\ 1966}}$	$\dfrac{\dot{q}_{AERO}}{\dot{q}_{FM\ MESA}}$	$\dfrac{\dot{q}_{AERO}}{\dot{q}_{NFM\ 1966}}$	$\dfrac{\dot{q}_{AERO}}{\dot{q}_{NFM\ MESA}}$	ϕ
180.0	0	1.82	0.195	0	19.85	Data	19.23	Data	0	Data	0	Data	0.969
175.0	0	1.67	0.196	3.81	23.98	Not	23.07	Not	0.16	Not	0.17	Not	0.962
169.9	0	1.50	0.197	9.14	29.21	Available	27.87	Available	0.31	Available	0.33	Available	0.954
165.2	0	1.34	0.198	15.64	35.35	For	33.37	For	0.44	For	0.47	For	0.944
160.2	0	1.15	0.199	24.97	44.09	This	41.05	This	0.57	This	0.61	This	0.931
155.0	0	0.930	0.200	38.02	55.98	Orbit	51.05	Orbit	0.68	Orbit	0.74	Orbit	0.912
150.0	0	0.713	0.201	54.57	72.00		63.86		0.76		0.85		0.887
144.9	0	0.442	0.202	76.23	95.51		81.37		0.80		0.94		0.852
140.0	0	0.126	0.203	102.30	128.71		104.00		0.79		0.98		0.808
138.0	0	0.088	0.204	114.59	147.24		115.29		0.78		0.99		0.783
135.8	0	0	0.204	129.31	171.67		128.75		0.75		1.00*		0.750
135.9	0	0	0.204	128.59	170.64		128.66		0.75		1.00*		0.754
138.0	0	0	0.204	114.59	146.99		115.39		0.78		0.99		0.785
140.0	0	0	0.203	102.30	128.84		104.36		0.79		0.98		0.810
145.0	0	0	0.202	75.75	94.86		81.58		0.80		0.93		0.860
150.1	0	0	0.201	54.19	71.89		64.27		0.75		0.84		0.894
154.8	0	0	0.200	38.59	56.40		51.66		0.68		0.75		0.916
159.9	0	0	0.199	25.62	44.56		41.62		0.57		0.62		0.934
164.9	0	0	0.198	16.13	35.85-		33.95		0.45		0.48		0.947
170.0	0	0	0.196	9.01	29.11		27.89		0.31		0.32		0.958
175.1	0	0	0.195	3.72	23.90		23.09		0.16		0.16		0.966
180.1	0	0	0.194	0	19.80		19.25		0		0		0.972

*Indicates that density from the 1966 Standard Atmosphere is inadequate for this orbit.

54

Table 7
Static and Dynamic Flight Parameters for Orbit 1558

Altitude (km)	ρ_∞ (kg/m³)	T_∞ (K)	M (kg/kgmole)	λ_∞ (m)	Kn_∞	U (m/s)	C_{mp} (m/s)	S_∞	T_o/T_∞	S_o	λ_o (m)	Kn_o	$\overline{V}$ (m/s)
180.3	6.132×10^{-10}	881.4	23.80	108.87	80.05	8587	784.8	10.94	32.03	1.93	74.12	54.50	885.3
174.9	7.462×10^{-10}	862.0	24.05	90.43	66.49	8597	771.9	11.14	33.17	1.93	61.57	45.27	870.7
170.2	8.944×10^{-10}	842.7	24.28	76.16	56.00	8600	759.7	11.32	34.92	1.92	52.03	38.26	856.9
165.1	1.099×10^{-9}	818.3	24.53	62.60	46.03	8603	744.8	11.55	36.31	1.92	42.77	31.45	840.1
159.9	1.374×10^{-9}	789.7	24.77	50.58	37.19	8607	728.0	11.82	37.98	1.92	34.56	25.41	821.2
155.0	1.725×10^{-9}	758.8	25.01	40.67	29.90	8617	710.3	12.13	40.74	1.90	27.97	20.57	801.2
149.9	2.227×10^{-9}	721.5	25.27	31.83	23.40	8619	689.1	12.51	43.27	1.90	21.89	16.10	777.3
145.0	2.910×10^{-9}	680.5	25.51	24.59	18.08	8622	666.0	12.95	46.29	1.90	16.92	12.44	751.2
140.0	3.943×10^{-9}	632.3	25.76	18.33	13.48	8637	638.9	13.52	51.33	1.89	12.65	9.30	720.7
138.9	4.230×10^{-9}	619.0	25.82	17.13	12.60	8634	631.3	13.68	52.53	1.89	11.82	8.69	712.1
140.0	3.943×10^{-9}	632.3	25.76	18.33	13.48	8639	638.9	13.52	51.33	1.89	12.65	9.30	720.7
145.0	2.910×10^{-9}	680.5	25.51	24.59	18.08	8630	666.0	12.96	46.36	1.90	16.92	12.44	751.2
149.9	2.227×10^{-9}	721.5	25.27	31.83	23.40	8623	689.1	12.51	43.27	1.90	21.89	16.10	777.3
155.1	1.718×10^{-9}	759.4	25.01	40.83	30.02	8611	710.6	12.12	40.67	1.90	28.08	20.65	801.6
160.0	1.369×10^{-9}	790.4	24.77	50.76	37.32	8607	728.4	11.82	37.98	1.92	34.68	25.50	821.6
165.2	1.094×10^{-9}	818.7	24.52	62.88	46.24	8600	745.1	11.54	36.25	1.92	42.96	31.59	840.5
170.2	8.944×10^{-10}	842.7	24.28	76.16	56.00	8604	759.7	11.33	34.98	1.92	52.03	38.26	856.9
174.9	7.462×10^{-10}	862.0	24.05	90.43	66.49	8595	771.9	11.13	33.12	1.93	61.57	45.27	870.7
180.3	6.132×10^{-10}	881.4	23.80	108.87	80.05	8588	784.8	10.94	32.03	1.93	74.12	54.50	885.3

(Left-side row group labels: DOWNLEG / UPLEG)

Table 7 (Continued)

Altitude (km)	ν_∞ (m²/s)	$R_{E\infty}$	C_v/R	C_p/R	γ	k_∞ (W/m K)	h^* (W/m² K)	$h_\infty/\overline{\alpha}$ (W/m² K)	T_R/T_∞	r	T_w/T_∞	T_w/T_o
180.3	32127.5	0.36	2.83	3.83	1.35	0.0195	0	0.0019	36.80	1.15	0.31	0.0097
174.9	26245.8	0.45	2.82	3.82	1.35	0.0191	0.00035	0.0023	38.11	1.15	0.32	0.0096
170.2	21753.8	0.54	2.80	3.80	1.36	0.0187	0.00082	0.0028	40.25	1.16	0.33	0.0095
165.1	17530.1	0.67	2.78	3.78	1.36	0.0182	0.0015	0.0033	41.85	1.16	0.35	0.0096
159.9	13845.4	0.85	2.76	3.76	1.36	0.0176	0.0025	0.0041	43.78	1.16	0.37	0.0097
155.0	10861.6	1.08	2.73	3.73	1.37	0.0170	0.0035	0.0051	47.10	1.16	0.39	0.0096
149.9	8247.2	1.42	2.70	3.70	1.37	0.0163	0.0049	0.0064	50.02	1.16	0.42	0.0097
145.0	6157.3	1.90	2.67	3.67	1.37	0.0156	0.0065	0.0082	53.52	1.16	0.46	0.0099
140.0	4403.5	2.67	2.64	3.64	1.38	0.0148	0.0081	0.0110	59.53	1.16	0.52	0.0101
138.9	4066.1	2.89	2.63	3.63	1.38	0.0146	0.0086	0.0117	60.92	1.16	0.54	0.0103
140.0	4403.5	2.67	2.64	3.64	1.38	0.0148	0.0081	0.0110	59.53	1.16	0.53	0.0103
145.0	6157.3	1.91	2.67	3.67	1.37	0.0156	0.0065	0.0082	53.60	1.16	0.49	0.0106
149.9	8247.2	1.42	2.70	3.70	1.37	0.0163	0.0049	0.0064	50.02	1.16	0.45	0.0104
155.1	10909.8	1.07	2.73	3.73	1.37	0.0170	0.0035	0.0051	47.02	1.16	0.42	0.0103
160.0	13901.5	0.84	2.76	3.76	1.36	0.0176	0.0025	0.0041	43.78	1.16	0.40	0.0105
165.2	17616.9	0.66	2.78	3.78	1.36	0.0182	0.0015	0.0033	41.78	1.16	0.38	0.0105
170.2	21753.8	0.54	2.80	3.80	1.36	0.0187	0.00082	0.0028	40.32	1.16	0.36	0.0103
174.9	26245.8	0.45	2.82	3.82	1.35	0.0191	0.00035	0.0023	38.05	1.15	0.35	0.0106
180.3	32127.5	0.36	2.83	3.83	1.35	0.0195	0	0.0019	36.80	1.15	0.34	0.0106

(Left margin labels: DOWNLEG / UPLEG)

Table 7 (Continued)

Altitude (km)	$\dot q_{SOLAR}$ (mW/cm²)	$\dot q_{ALBEDO}$ (mW/cm²)	$\dot q_{IR}$ (mW/cm²)	$\dot q_{AERO}$ (mW/cm²)	$\dot q_{FM\ 1966}$ (mW/cm²)	$\dot q_{FM\ MESA}$ (mW/cm²)	$\dot q_{NFM\ 1966}$ (mW/cm²)	$\dot q_{NFM\ MESA}$ (mW/cm²)	$\dfrac{\dot q_{AERO}}{\dot q_{FM\ 1966}}$	$\dfrac{\dot q_{AERO}}{\dot q_{FM\ MESA}}$	$\dfrac{\dot q_{AERO}}{\dot q_{NFM\ 1966}}$	$\dfrac{\dot q_{AERO}}{\dot q_{NFM\ MESA}}$	ϕ
180.3	0	8.92	0.196	0	19.41	19.63	18.83	19.04	0	0	0	0	0.970
174.9	0	8.78	0.197	3.59	23.71	24.78	22.83	23.86	0.15	0.14	0.16	0.15	0.963
170.2	0	8.63	0.198	8.70	28.44	30.75	27.16	29.37	0.30	0.28	0.32	0.30	0.955
165.1	0	8.46	0.200	16.46	34.99	39.80	33.07	37.61	0.47	0.41	0.50	0.44	0.945
159.9	0	8.26	0.200	26.98	43.80	51.65	40.78	48.09	0.62	0.52	0.66	0.56	0.931
155.0	0	8.04	0.201	39.50	55.18	69.42	50.38	63.38	0.72	0.57	0.78	0.62	0.913
149.9	0	7.73	0.202	55.42	71.30	94.44	63.39	83.96	0.78	0.59	0.87	0.66	0.889
145.0	0	7.34	0.203	73.64	93.26	129.79	79.83	111.10	0.79	0.57	0.92	0.66	0.856
140.0	0	6.63	0.204	95.39	127.02	186.52	102.76	150.89	0.75	0.51	0.93	0.63	0.809
138.9	0	5.99	0.205	100.63	136.13	189.87	108.50	151.33	0.74	0.53	0.93	0.66	0.797
140.0	0	5.45	0.205	95.39	127.11	167.96	103.09	136.22	0.75	0.57	0.93	0.70	0.811
145.0	0	4.60	0.204	73.64	93.52	123.40	80.52	106.25	0.79	0.60	0.91	0.69	0.861
149.9	0	4.05	0.203	55.42	71.39	92.97	63.75	83.02	0.78	0.60	0.87	0.67	0.893
155.1	0	3.58	0.202	39.22	54.85	69.92	50.35	64.19	0.71	0.56	0.78	0.61	0.918
160.0	0	3.21	0.201	26.76	43.64	53.56	40.80	50.08	0.61	0.50	0.66	0.53	0.935
165.2	0	2.87	0.199	16.30	34.79	41.34	32.98	39.19	0.47	0.39	0.49	0.42	0.948
170.2	0	2.56	0.198	8.70	28.48	32.48	27.28	30.79	0.30	0.27	0.32	0.28	0.958
174.9	0	2.29	0.197	3.59	23.69	25.94	22.88	25.06	0.15	0.14	0.16	0.14	0.966
180.3	0	2.02	0.196	0	19.42	20.30	18.90	19.75	0	0	0	0	0.973

DOWNLEG

UPLEG

Table 8

Static and Dynamic Flight Parameters for Orbit 2271

	Altitude (km)	ρ_∞ (kg/m³)	T_∞ (K)	M (kg/kgmole)	λ_∞ (m)	Kn_∞	U (m/s)	C_{mp} (m/s)	S_∞	T_o/T_∞	S_o	λ_o (m)	Kn_o	$\bar{V}$ (m/s)
D	179.9	6.206×10^{-10}	880.2	23.81	107.64	79.15	8476	784.0	10.81	31.30	1.93	73.28	53.88	884.4
O	175.0	7.427×10^{-10}	862.5	24.05	90.84	66.79	8482	772.2	10.98	32.26	1.93	61.85	45.48	871.0
W	169.9	9.045×10^{-10}	841.2	24.29	75.35	55.40	8483	758.8	11.18	34.09	1.91	51.63	37.96	855.9
N	165.0	1.104×10^{-9}	817.9	24.53	62.33	45.83	8498	744.6	11.41	35.46	1.92	42.58	31.31	839.9
L	160.0	1.369×10^{-9}	790.4	24.77	50.76	37.32	8496	728.4	11.66	36.99	1.92	34.68	25.50	821.6
E	155.0	1.725×10^{-9}	758.8	25.01	40.67	29.90	8499	710.3	11.97	39.70	1.90	27.97	20.57	801.2
G	150.1	2.207×10^{-9}	723.1	25.26	32.10	23.60	8511	690.0	12.33	42.06	1.90	22.08	16.24	778.3
	155.0	1.725×10^{-9}	758.8	25.01	40.67	29.90	8506	710.3	11.98	39.76	1.90	27.97	20.57	801.2
U	160.0	1.369×10^{-9}	790.4	24.77	50.76	37.32	8504	728.4	11.67	37.05	1.92	34.68	25.50	821.6
P	165.0	1.104×10^{-9}	817.9	24.53	62.33	45.83	8497	744.6	11.41	35.46	1.92	42.58	31.31	839.9
L	169.9	9.045×10^{-10}	841.2	24.29	75.35	55.40	8491	758.8	11.19	34.15	1.91	51.63	37.96	855.9
E	174.9	7.462×10^{-10}	862.0	24.05	90.43	66.49	8486	771.9	10.99	32.31	1.93	61.57	45.27	870.7
G	180.1	6.164×10^{-10}	880.8	23.81	108.34	79.66	8484	784.4	10.82	31.35	1.93	73.76	54.24	884.8

Table 8 (Continued)

Altitude (km)	ν_∞ (m²/s)	R_{E_∞}	C_v/R	C_p/R	γ	k_∞ (W/m K)	h^* (W/m² K)	$h_\infty/\bar{\alpha}$ (W/m² K)	T_R/T_∞	r	T_W/T_∞	T_W/T_o
179.9	31732.3	0.36	2.83	3.83	1.35	0.0195	0	0.0019	35.96	1.15	0.29	0.0093
175.0	26373.9	0.44	2.82	3.82	1.35	0.0191	0.00050	0.0023	37.06	1.15	0.29	0.0090
169.9	21497.4	0.54	2.80	3.80	1.36	0.0186	0.0010	0.0028	39.29	1.16	0.30	0.0088
165.0	17450.3	0.66	2.78	3.78	1.36	0.0182	0.0015	0.0033	40.87	1.16	0.32	0.0090
160.0	13901.5	0.83	2.76	3.76	1.36	0.0176	0.0021	0.0040	42.63	1.16	0.33	0.0089
155.0	10861.6	1.06	2.73	3.73	1.37	0.0170	0.0029	0.0050	45.89	1.16	0.35	0.0088
150.1	8327.8	1.39	2.71	3.71	1.37	0.0164	0.0039	0.0063	48.63	1.16	0.39	0.0093
155.0	10861.6	1.07	2.73	3.73	1.37	0.0170	0.0029	0.0050	45.97	1.16	0.37	0.0093
160.0	13901.5	0.83	2.76	3.76	1.36	0.0176	0.0021	0.0041	42.70	1.16	0.36	0.0097
165.0	17450.3	0.66	2.78	3.78	1.36	0.0182	0.0015	0.0033	40.87	1.16	0.34	0.0096
169.9	21497.4	0.54	2.80	3.80	1.36	0.0186	0.0010	0.0028	39.35	1.16	0.33	0.0097
174.9	26245.8	0.44	2.82	3.82	1.35	0.0191	0.00051	0.0023	37.13	1.15	0.32	0.0099
180.1	31953.1	0.36	2.83	3.83	1.35	0.0195	0	0.0019	36.02	1.15	0.33	0.0105

(Left margin labels reading vertically: DOWNLEG for the upper rows and UPLEG for the lower rows)

Table 8 (Continued)

Altitude (km)	$\dot{q}_{SOLAR}$ (mW/cm^2)	$\dot{q}_{ALBEDO}$ (mW/cm^2)	$\dot{q}_{IR}$ (mW/cm^2)	$\dot{q}_{AERO}$ (mW/cm^2)	$\dot{q}_{FM\ 1966}$ (mW/cm^2)	$\dot{q}_{FM\ MESA}$ (mW/cm^2)	$\dot{q}_{NFM\ 1966}$ (mW/cm^2)	$\dot{q}_{NFM\ MESA}$ (mW/cm^2)	$\dfrac{\dot{q}_{AERO}}{\dot{q}_{FM\ 1966}}$	$\dfrac{\dot{q}_{AERO}}{\dot{q}_{FM\ MESA}}$	$\dfrac{\dot{q}_{AERO}}{\dot{q}_{NFM\ 1966}}$	$\dfrac{\dot{q}_{AERO}}{\dot{q}_{NFM\ MESA}}$	ϕ
179.9	0	0	0.194	0	18.90	15.62	18.31	15.14	0	0	0	0	0.969
175.0	0	0	0.195	4.98	22.66	19.53	21.80	18.79	0.22	0.25	0.23	0.26	0.962
169.9	0	0	0.196	10.40	27.61	25.00	26.31	23.82	0.38	0.42	0.40	0.44	0.953
165.0	0	0	0.197	15.79	33.88	31.91	31.95	30.09	0.47	0.49	0.49	0.52	0.943
160.0	0	0	0.198	22.44	41.98	41.09	38.96	38.13	0.53	0.55	0.58	0.59	0.928
155.0	0	0	0.200	31.18	52.95	54.33	48.13	49.39	0.59	0.57	0.65	0.63	0.909
150.1	0	0	0.201	42.72	68.03	71.52	60.34	63.44	0.63	0.60	0.71	0.67	0.887
155.0	0	0	0.200	31.18	53.08	55.70	48.41	50.80	0.59	0.56	0.64	0.61	0.912
160.0	0	0	0.199	22.44	42.10	43.05	39.24	40.12	0.53	0.52	0.57	0.56	0.932
165.0	0	0	0.198	15.79	33.86	33.74	32.00	31.88	0.47	0.47	0.49	0.50	0.945
169.9	0	0	0.198	10.40	27.68	26.87	26.46	25.69	0.38	0.39	0.39	0.40	0.956
174.9	112.08	0	0.197	5.08	22.80	21.51	21.98	20.74	0.22	0.24	0.23	0.24	0.964
180.1	112.57	0	0.196	0	18.82	—	18.29	—	0	0	0	0	0.972